SURF ZONE SEDIMENT SIZE VARIATION, MORPHODYNAMICS, AND HYDRODYNAMICS DURING SEA/LAND BREEZE AND EL-NORTE STORM IN SISAL, YUCATAN, MEXICO

A Thesis

by

TARIQ I S I ALRUSHAID

Submitted to the Office of Graduate and Professional Studies of
Texas A&M University
in partial fulfillment of the requirements for the degree of

MASTER OF SCIENCE

Chair of Committee,	Timothy Dellapenna
Committee Members,	Jens Figlus
	Pete van Hengstum
Head of Department,	Debbie Thomas

August 2015

Major Subject: Oceanography

ABSTRACT

This study compares the effects of a mesoscale pressure system (i.e., cold front: referred to as El-Norte) and local pressure systems (land and sea breezes) on the hydrodynamics, beach profile, and particle size distribution of sediments within the surf zone. The effect of onshore and offshore wind has been investigated using measurements of hydrodynamics (water elevation, current velocities and direction), geomorphology (surface sediment samples and beach profiles), and meteorological observations (wind, temperature and atmospheric pressure). The experiment was conducted on Sisal beach located in the Gulf of Mexico along the northern coast of the Yucatan Peninsula from March 27th 2014 to April 11th 2014. For a 50 m cross section of the beach (i.e., the surf zone) hydrodynamics were analyzed by estimating turbulent kinetic energy, kinetic energy dissipation rate and bed shear stress using the measurements obtained from Acoustic Doppler Velocimeters (ADV). Significant wave height and wave period in the surf zone were computed using pressure sensors from ADVs. A pressure transducer located in the swash zone provided additional water free-surface elevation data to help assess wave energy dissipation.

During sea breeze cycles with wind velocities reaching up to 15 ms^{-1}, rapid changes in wave height over a short period of time were observed. One *El-Norte* storm event affected the study site during the field campaign with maximum wind speeds of 15 ms^{-1}, and significant wave heights of 1.5 m and 0.3 m in water depths of 10 m and 0.4 m, respectively. This study will test five hypotheses: (1) El-Norte is more effective in

skewing sediment size distributions toward coarser grain sizes compared to regular sea-breeze events, (2) sea-breeze events result in deposition of sediment within the surf zone and erosion in the swash zone, in addition to onshore sandbar migration, (3) an individual El-Norte event can cause significant alterations to the beach profile resulting in a steeper beach profile and significant erosion in the swash zone and surf zone, (4) the undertow currents are stronger during El-Norte than during sea/land-breezes and play an important role in the offshore sandbars migration.

ACKNOWLEDGEMENTS

I would like to thank my committee chair, Dr. Timothy Dellapenna, and my committee members, Dr. Jens Figlus, and Dr. Pete van Hengstum, for their guidance and support throughout the course of this research.

I would like to also thank my friends and colleagues and the department faculty and staff for making my time at Texas A&M University a great experience. A special thanks to my colleagues Dr. Fahad Al Senafi and Mohamad Al Mukaimi for their help and support. I am very grateful to Miss Nina Wellmann for her help with processing the sediment samples.

I also want to extend my gratitude to the Institute of Engineering at the National Autonomous University of Mexico (UNAM) for their support of the field experiment. The project PIs Dr. Alec Torres-Freyermuth (UNAM) and Dr. Jack Puleo (University of Delaware) deserve a special thank you for organizing this international collaboration. Furthermore, I would like to thank everyone involved in the data collection efforts.

Finally, thanks to my mother and father for their encouragement and their warm words that helped me during the tough times, and to my beautiful wife Nora and my daughter Loura and my son Rusheed for their patience and love.

NOMENCLATURE

ADCP	Acoustic Doppler Current Profiler	
ADV	Acoustic Doppler Velocimeter	
CCP	Conductive Concentration Profiler	
DGPS	Differential Global Positioning System	
EMCM	Electromagnetic Current Meters	
LB	Land-Breeze	
OBS	Optical Backscatter Sensor	
PT	Pressure Transducer	
SB	Sea-Breeze	
C_D	Wind Drag Coefficient	Dimensionless
d_{50}	Median Sediment Diameter	mm
H	Wave Height	m
$\overline{H}$	Mean Zero Crossing Wave Height	m
H_s	Significant Wave Height	m
k	Empirical Von Kármán Constant	Dimensionless
M_{total}	Total Mass	%
$m_{retained}$	Mass of Sediment Retained	g
m_{total}	Total Mass of The Sample	g

$M_{d\phi}$	Mean Diameter	
P	Pressure	Nms^{-2}
ρ	Water Density	Kgm^{-3}
T	Wave Period	s
T	Mean Zero Crossing Period	s
T_s	Significant Wave Period	s
τ_b	Bed Shear Stress	Nm^{-2}
τ_w	Wind Stress	Nm^{-2}
TKE	Turbulent Kinetic Energy	m^2s^{-2}
u	Velocity in The X Direction	ms^{-1}
u_*	Frictional Velocity	ms^{-1}
U_h	Wind Speed at a Reference Height	ms^{-1}
v	Velocity in The Y Direction	ms^{-1}
w	Velocity in The Z Direction	ms^{-1}
z	Vertical Distance	m
σ_ϕ	Standard Deviation	
α_ϕ	Skewenss	
ϕ	Phi	
ε	Turbulent Kinetic Energy (TKE) Dissipation Rate	m^2s^{-3}

TABLE OF CONTENTS

Page

LIST OF FIGURES

Page

Page

Page

LIST OF TABLES

1. INTRODUCTION

1.1. Motivation, and objectives

Coastal regions are highly dynamic physical systems, where accretion/erosion occurs frequently, especially in the inner and outer surf zone due to high-energy dissipation [*Dolan et al.*, 1978]. Coastal erosion can be a result from chronic processes at multiple time scales, such as long-term sea-level rise [*Brammer*, 2014; *Esteves et al.*, 2002; *Hinkel et al.*, 2013], ephemeral hurricanes [*Conner et al.*, 1989; *Esteves et al.*, 2002], mesoscale extra-tropical cyclones [*Dingler and Reiss*, 1990; *Esteves et al.*, 2002], or from cumulative sea-breezes effect [*Pattiaratchi et al.*, 1997; *Sonu et al.*, 1973]. Wind stress is the main mechanism that drives energy and momentum to the ocean (i.e., formation of surface gravity waves) [*Babanin*, 2011; *Kinsman*, 1965]. Strong wave events resulting from tropical or extratropical cyclones can dramatically impact coastal regions on short time scales. However, *Sonu et al.* [1973] suggest that the cumulative effect of a diurnal wind system, such as sea-breeze, can cause significant modification to the coastal region.

Wave hydrodynamics in the surf zone can be altered depending on the direction and magnitude of the sea-breeze [*Sonu et al.*, 1973]. As the waves enter the surf zone, turbulence increases and more energy is dissipated due to bottom friction. This energy can be enhanced when sea-breeze is present in the region. *Pattiaratchi et al.* [1997] performed a study on a sandy beach located in southwestern Australia and observed a

significant impact on the rate of littoral sediment transport due to an increase in current velocity and significant energy dissipation during sea-breeze events.

In order to understand more about the effect of cold fronts and sea/land-breezes on coastal regions, it is essential to observe the meteorological and hydrodynamic forcing that drives sediment processes within the surf and swash zones, both on temporal and spatial scales. Therefore, a field experiment was designed to collect measurements and diagnose the relative effects of cold fronts versus sea/land-breezes in coastal regions. The study site was selected because it is characterized by a diurnal sea-breeze climate with cold fronts during winter, referred to as El-Norte, and tropical storms during the summer, which provide a good comparison to their effect on the coastal region.

In the surf zone, several processes (e.g., increase in wave height and/or increase in the cross/longshore currents) contribute to sediment transport; re-suspension and distribution; and coastal morphological change. This study will compare the effects of mesoscale pressure systems (i.e., cold fronts and local pressure systems) in the surf zone, with a particular focus on the impact of particle size distributions and beach profile. The study will test the following hypotheses:

I. El-Norte is more effective in skewing sediment size distributions toward coarser grain sizes compared to regular sea-breeze events.

II. Sea-breeze events result in deposition of sediment within the surf zone and erosion in the swash zone, in addition to onshore sandbar migration.

III. An individual El-Norte event can cause a steeper beach profile and significant erosion in the swash zone and surf zone.

IV. The undertow currents are stronger during El-Norte than during sea/land-breezes and play an important role in the migration of offshore sandbars.

1.2. Literature review

1.2.1. Cold fronts

A cold front (i.e., extratropical cyclones) can be defined as a cold air mass propagating over a warmer surface, which can be land or sea [*Miller and Thompson*, 1970]. *Gallucci and Netto* [2005] found that the effects of cold fronts in reshaping costal regions can be significant, due to high wind stress amplitudes as a result from atmospheric disturbance [*Stech and Lorenzzetti*, 1992]. For instance, both *Dragani* [1999] and *Gallucci and Netto* [2005] found cold fronts to be a source of ocean surface turbulent kinetic energy, which is one mechanism to suspended sediments. In addition, *Stone et al.* [2004] suggested that cold fronts are one of the key factors affecting coastline migration. In South America, cold fronts are common climate events that are found during the whole year, however, their periodicity increases during the winter seasons up to 40, with wind velocities ranging between 8 to 20 ms^{-1} [*Brinkkemper et al.*, 2013; *Curtarelli et al.*, 2013; *Gallucci and Netto*, 2005; *Garreaud*, 2000; *Salles et al.*, 2013; *Stech and Lorenzzetti*, 1992].

In the Gulf of Mexico (GOM), both extratropical and tropical (i.e., hurricanes) cyclones can impact coastal sedimentary processes [Rutecki *et al.*, 2014]. Although hurricanes can mobilize tremendous volumes of sediment in the coastal zone [*Dickey et al.*, 1998; *Dolan et al.*, 1978; *Miner et al.*, 2009], the higher frequency of cold fronts may in fact cause greater cumulative effects on sediment transport and the coastal region

[*Moeller et al.,* 1993; *Roberts et al.*, 1987]. *Moeller et al.* [1993] investigated how cold fronts impact a microtidal beach and found that deposition and erosion occurred on different parts of the coast, as wave setup and wave action increased during the storm. *Stone et al.* [2004] stated that shallow waters with microtidal currents do not play a significant role in suspending sediments. During the passage of cold fronts, higher waves break over the sandbars resulting in strong offshore currents which eventually drive the offshore migration of the sandbars [*Hoefel and Elgar*, 2003].

In addition, *Kineke et al.* [2006] concluded that onshore cold fronts are able to transport fine sediments from the shallow inner shelf to the coast due to increased wave energy and high suspended sediment concentrations. *Kobashi et al.* [2007] found that during pre-offshore cold fronts mud deposition occurred offshore, while post cold front hydrodynamic processes resulted in erosion of the deposited mud and skewed size distributions to coarser sediment due to the increase in wave height and bottom shear stress.

1.2.2. Sea-breeze and land-breeze

Land and sea-breeze are common atmospheric processes that occur globally [*Masselink and Pattiaratchi*, 1998]. However, sea-breeze systems mostly develop between 20^{o} and 35^{o} latitude due to weaker trade wind systems in these areas [*Inman and Filloux*, 1960; *Pattiaratchi et al.*, 1997]. Sea-breeze is a stable diurnal system, generated due to thermal temperature variation between land and sea [*Hsu*, 1988; *Pattiaratchi et al.*, 1997; *Sonu et al.*, 1973]. *Masselink and Pattiaratchi* [1998] suggested that sea-breeze is more common in regions characterized by low wave energy and

microtidal environment. The magnitude of the sea-breeze depends on the temperature differences between the land and sea [*Hsu*, 1988]. *Masselink and Pattiaratchi* [1998] also suggested that significant sea-breeze impact on coastal areas is more common during hot summer days. Land-breeze is known to be weaker than sea-breeze, due to topography roughness, and the lack of air convection, which prevent it from building up stronger winds [*Sonu et al.*, 1973].

During sea-breeze conditions nearshore currents increase significantly. The maximum longshore current velocity observed by *Pattiaratchi et al.* [1997] reached $3.1 ms^{-1}$. In addition, studies observed that sea-breeze results in increasing significant wave height (H_s), wave period (T_s), and maximum runup level [*Inman and Filloux*, 1960; *Masselink and Pattiaratchi*, 1998; *Pattiaratchi et al.*, 1997]. Several studies have been conducted on the impact of sea-breeze on coastal regions, and specifically beach morphology and sediment transport, where it has been noted that sea-breeze plays an important role in controlling littoral sand transport and morphological changes on sandy beaches [*Masselink and Pattiaratchi*, 1998; *Pattiaratchi et al.*, 1997; *Sonu et al.*, 1973]. Furthermore, results by *Sonu et al.* [1973], *Pattiaratchi et al.* [1997] and *Masselink and Pattiaratchi* [1998] showed that sea-breeze events are associated with changes in beach profiles, erosion of the beach-face, and deposition of sediment offshore. *Masselink and Pattiaratchi* [1998], related beach morphodynamic changes directly to the increased wave energy and current velocities generated from sea-breeze events.

1.2.3. Beaches and coastal processes

Nearshore coastal regions are considered important because they are the primary area for beach recreation and help to boost the local economy [*Senechal et al.*, 2015]. The beach profile can be divided into 3 regions: offshore, nearshore zone, beach/shore, and the coast [*Dean and Dalrymple*, 2002] (see Figure 1). Waves coming from the offshore region will become unstable and start to break at the breaker zone, where sandbars usually exist. The surf zone starts with the breaker zone, where the waves break and form onshore directed bores. The third region that is affected by the waves is the beach face (swash zone), since it is covered by water during the run-up and exposed during the backwash.

Several studies have focused on beach grain size distributions [*Abuodha*, 2003; *Rajganapathi et al.*, 2012; *Wang et al.*, 1998], shapes of sediments [*Çelikoğlu et al.*, 2006; *Rajganapathi et al.*, 2012; *Türker and Kabdaşlı*, 2006], cross-shore beach profile [*Feng et al.*, 2007; *Karunarathna et al.*, 2012b; *Karunarathna et al.*, 2014], and the effect of hydrodynamics on nearshore processes [*Houser and Greenwood*, 2007; *Senechal et al.*, 2015; *Ting and Kirby*, 1996; *Wang et al.*, 1998]. Observations of grain size distributions within the surf zone are essential for studying cross-shore sediment transport and beach morphology [*Wang et al.*, 1998].

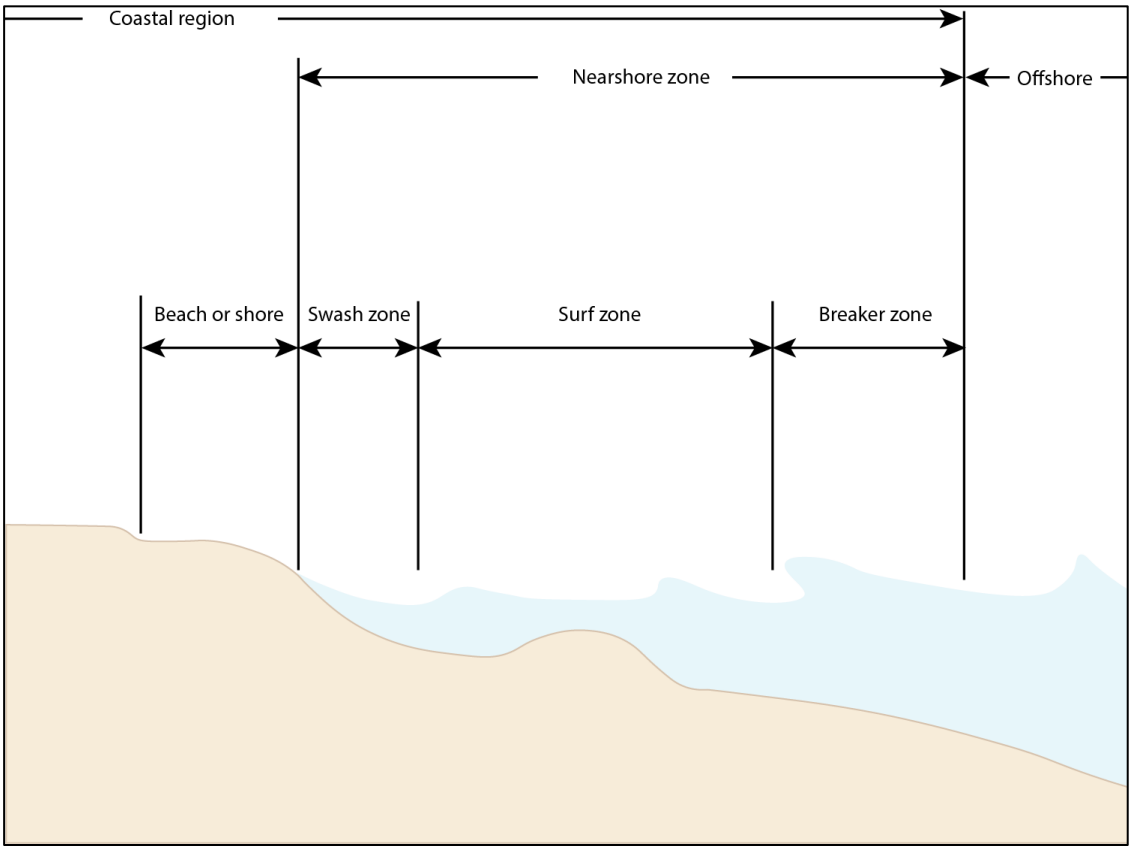

Figure 1. Beach profile terminology (adapted from *Dean and Dalrymple* [2002]).

Grain size statistics (e.g., mean, skewness, and kurtosis) can be used to assess the predominant wave energy level. Vice-versa, *Wang et al.* [1998] and *Dean* [1991] suggested that by using the rate of wave energy dissipation, the distribution pattern of grain sizes can be determined. Turbulence generated by breaking waves is one of the important mechanisms that drives sediment transport and changes of beach profiles [*Ting and Kirby*, 1996]. It results in significant suspension of sediments, which then are transported in the cross-shore and alongshore direction by waves and currents.

One of the main factors controlling short-term beach profile changes is cross-shore sediment transport. However, longshore transport also contributes to sediment transport processes and can control the long-term changes [*Karunarathna et al.*, 2012b]. In addition, the cross-shore profile is affected by a number of parameters; wave energy within the region, tidal regime, magnitude of undertow currents, turbulence, and sediment characteristics [*Karunarathna et al.*, 2012a]. Sandy beaches are characterized by a gentle and wide slope, and a shallow surf zone [*Karunarathna et al.*, 2012a]. Sandbars are common coastal morphological features; their movement is dependent on the wave energy within the region. During storms with high wave energy, sandbars tend to move offshore [*Gallagher et al.*, 1998; *Houser and Greenwood*, 2007], while during low wave energy periods, sandbars tend to migrate landward [*Gallagher et al.*, 1998; *Houser and Greenwood*, 2007].

1.3. Turbulence

Turbulence can be defined as the processes where laminar flow becomes turbulent and moving in eddying motion [*Thorpe*, 2005]. Turbulence is accepted to be energetic, which plays an important role in vertical mixing of momentum, the flow, and sediment transport [e.g., *Wolfgang*, 1987; *Trowbridge and Elgar, 2001*]. Surf zone turbulence is produced on the surface due to wave breaking and on the bottom layer due to shear [*Feddersen,* 2012]. In order to understand the the effect of turbulence on the surf zone it is important to compute turbulence properties such as:

I. Bottom shear stress (τ_b): τ_b is one of key elements that drive sediment transport in a natural system and control erosion/deposition of sediment [*Feddersen et al.*,

2007; *Kim et al.*, 2000; *Pope et al.*, 2006]. τ_b depends on the frictional velocity, sometimes referred as shear velocity (u_*), where increasing the shear velocity will result in increasing τ_b. By using the von Karman Prandtl law for velocity distribution, shear velocity can be obtained and used to estimate bed shear stress. However, shear stress can also be obtained using turbulence measurements and estimated from Reynolds stress [*Biron et al.*, 1998; *Biron et al.*, 2004].

II. Turbulent kinetic energy (TKE): TKE is used in order to estimate the energy produced by turbulence, which can be estimated using the velocity fluctuation (explained in section 2.3.2). Most energetic processes in the coastal region take place in the neashore region. Due to the shallow depth the energy supplied by turbulence can cover the whole water column. As wave height increases TKE values increase as a result of turbulence produced by the breaking waves.

III. Turbulent kinetic energy dissipation rate (ε): ε is used to study turbulence within coastal and ocean waters [*Feddersen et al.*, 2007]. The braking wave energy will be dissipated via turbulence. In addition, the increase in ε will result in more sediment being eroded from the bed and carried away in suspension.

1.4. Study area

The study area is located in Sisal (21° 9'58.40"N 90° 2'11.00"W) along the northern coast of the Yucatan Peninsula (Figure 2). The coast of Yucatan is characterized by a wide continental shelf of approximately 245 km with a slope of 1/1000 [*Appendini et al.*, 2012; *Enriquez et al.*, 2010; *Mendoza et al.*, 2013]. Studies of Progreso beach (north-east of Sisal) reported that the coast is sandy with a mean grain

size between 0.2 mm to 0.5 mm (0.5 m depth and swash zone, respectively) and a poorly-sorted sediment size distribution [*Appendini et al.*, 2012; *Uc-Sánchez*, 2009]. Carbonate sediment is considered the dominant source in the northwest coast, where calcareous beach sediment is primarily derived from biogenic processes [*Jiménez and Ávila*, 2009], and abundent shell fragment were found in the swash zone (see Appendix 1). The region has a mixed tidal cycle with a tidal range of 0.1 m during neaps and 0.8 m during spring tides [*Appendini et al.*, 2012; *Mendoza et al.*, 2013; *Salles et al.*, 2013]. The area has high wave energy, due to the effect of the wind systems throughout the year [*Appendini et al.*, 2012]. Current velocities can reach 0.4 ms^{-1} during storms, and significant wave height (H_s) is usually less than 1 m in the surf zone [*Brinkkemper et al.*, 2013; *Salles et al.,* 2013].

The north coast of Yucatan is exposed to atmospheric circulations including: tropical cyclones, anticyclones, cold fronts propagating from the north (will be referred to as *El-Norte*) and a strong sea-breeze system [*Figueroa-Espinoza et al.*, 2014; *Mendoza et al.*, 2013]. The wind climate in Sisal shows a greater wind velocity which is 50% stronger compared to other locations within a 50 km radius [*Figueroa-Espinoza et al.*, 2014]. *Figueroa-Espinoza et al.* [2014] suggested that wind direction is almost consistent between northeasterly and southeasterly winds.

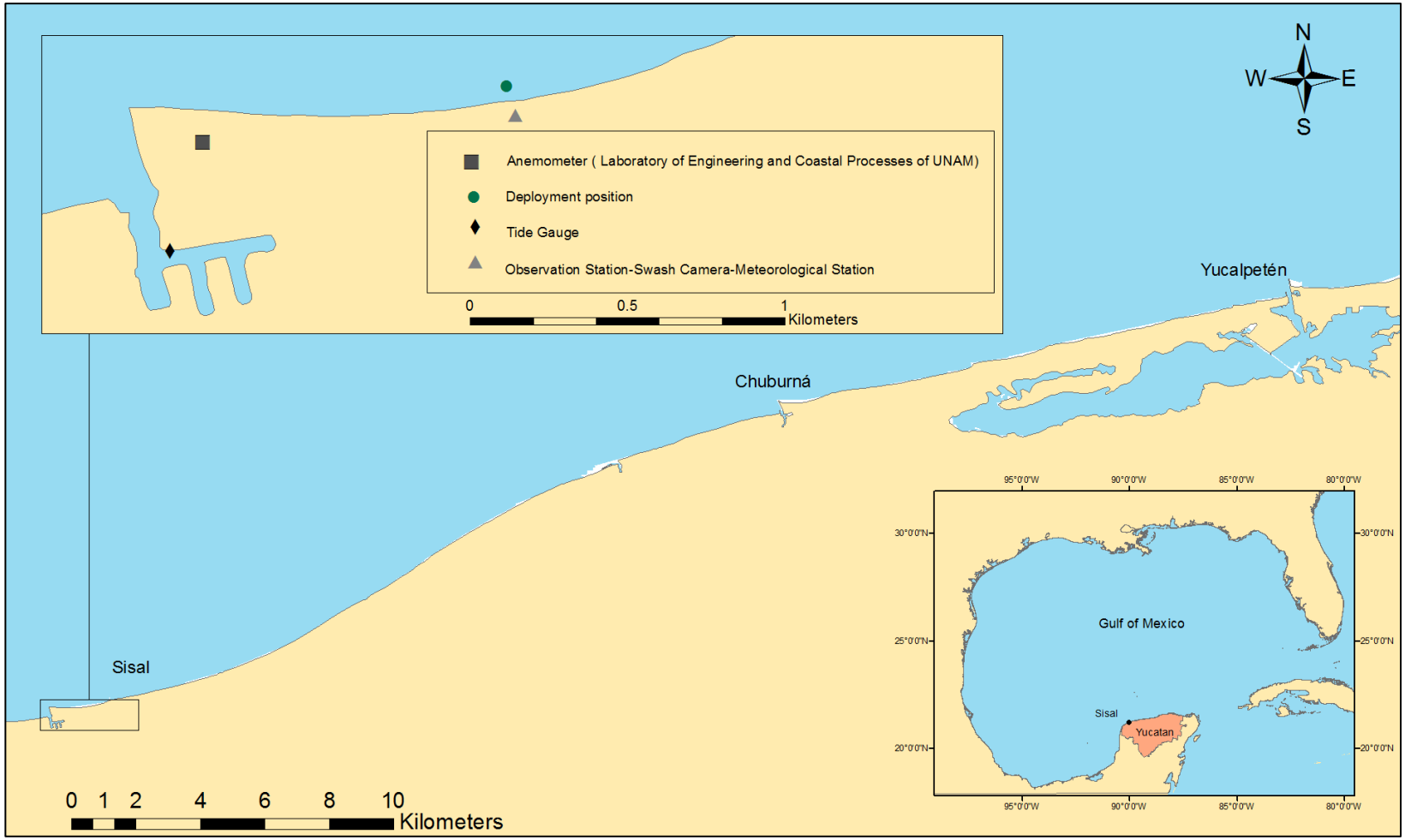

Figure 2. Map of the study area showing (a) location of Sisal on the Yucatan Peninsula, (b) a part of the northwest coast of the Yucatan Peninsula, and (c) study site with instrument locations.

2. METHODOLOGY

Field data acquisition was accomplished using more than 50 instruments from March 27th 2014 to April 12th 2014 on the beach of Sisal. However, the present study only focuses on three different wind scenarios that occurred between the April 1st and April 10th using some of the instruments located on the middle transect. The deployed instruments measured waves, currents, water elevation, meteorological data, and sediment concentrations and were positioned at different depths. The study area has been divided into three transect (west, middle and east transect) as shown in Figure 3 (landscape view of the transect can be obtained from appendix B).

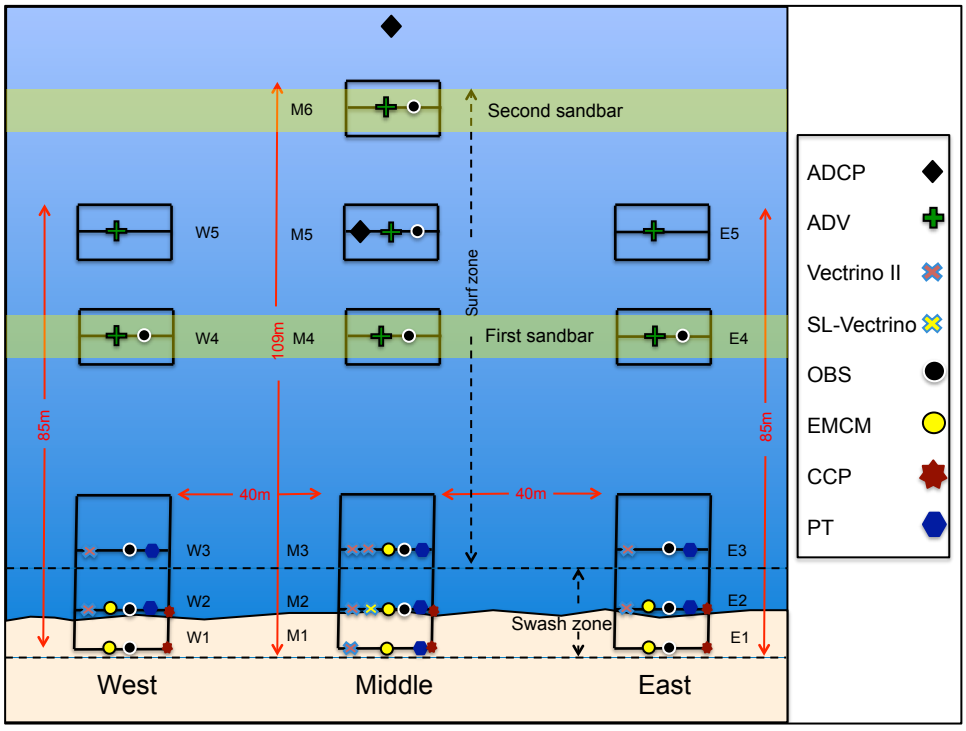

Figure 3. Schematics of the instrument setup for the East, Middle and West transects (Figure not drawn to scale).

2.1. Instrument setup

Two meteorological stations were located onshore near the study site. The first at a height of 10 m (Visual-Met) directly at the experiment site. An anemometer was placed east of the study site on the National Autonomous University of Mexico (UNAM) building at a height of 50 m, as shown in Figure 2. Both meteorological stations took measurements of wind speed (ms^{-1}), wind direction (degrees), temperature (C^{o}), humidity (%) and atmospheric pressure (Pa). The UNAM anemometer sampling frequency was 12 Hz, while the Visual-Met sampling frequency was 1 Hz. In addition, tidal observations were obtained from a tide gauge located in Sisal port (see Figure 2).

All the instruments in the swash zone were recording simultaneously via GPS synchronization. Water level measurements were obtained using 7 pressure transducers (PTs) with a sampling rate of 16 Hz (manufactured by Druck). Swash zone flows were measured with, 7 Vectrino II acoustic Doppler profiling velocimeters, installed on the first three frames of each transects. The velocimeters provided high-resolution velocity measurements in three components (*x, y* and *z*). These Vectrino II have the capability to measure velocity profiles over 30 mm above the bed (a measurement every 1 mm) at a sampling rate of 100 Hz. In addition, one side looking Vectrino acoustic Doppler velocimeter (SL-Vectrino) was placed on M2 (Figure 2). The SL-Vectrino head was positioned horizontally to provide a fixed-point velocity measurement in the horizontal plane with a sampling rate of 200 Hz. Both, the Vectrino II and SL-Vectrino, are used to obtain precise turbulence estimates associated with the wave bores in the swash zone.

Electromagnetic Current Meters (EMCM) were used to obtain 2D high-resolution velocity measurements (*x* and *y* component) within the swash zone.

Two offshore Acoustic Doppler Current Profiler (ADCP) were placed at water depths of 4m and 10m, respectively, and measured wave characteristics (wave height, period and direction) at 40-minute intervals. Eulerian velocity measurements, in the surf zone were collected by 7 Acoustic Doppler Velocimeters (ADV) sampling at a rate of 16 Hz.

Near-bed sediment transport was measured using 9 Conductive Concentration Profilers (CCP). CCPs have been used in several studies in the field (e.g. *Lanckriet et al.,* 2012 and *Lanckriet et al.,* 2013), but are not part of the investigation discussed in this paper. Measurements of sediment concentration within the water column were obtained using 13 Optical Backscatter Sensors (OBS), positioned on the first frames in the swash zone and next to each vector located within the surf zone.

Instruments located in the surf zone and Visual-Met, were synchronized by a GPS timer (UTC Time) and connected by cables to computers in a field trailer located near the study site (Figure 4). It is important to mention that the present study will only show data obtained from the ADVs, PTs, meteorological stations, surface sediment grab samples and beach profile measurements from the middle transect. Three events were chosen to be studied based on the wind observation obtained from Visual-Met; Land-Breeze (LB) from 12:00-18:00 April 3rd, Sea-Breeze (SB) from 20:00 April 3rd - 03:00 April 4th and El-Norte from 11:00 April 8th to 10:00 April 9th (visual images of wave conditions during each event are provided in appendix C). The period of LB and SB

events were chosen based on the quality of available data with no instruments being exposed to air.

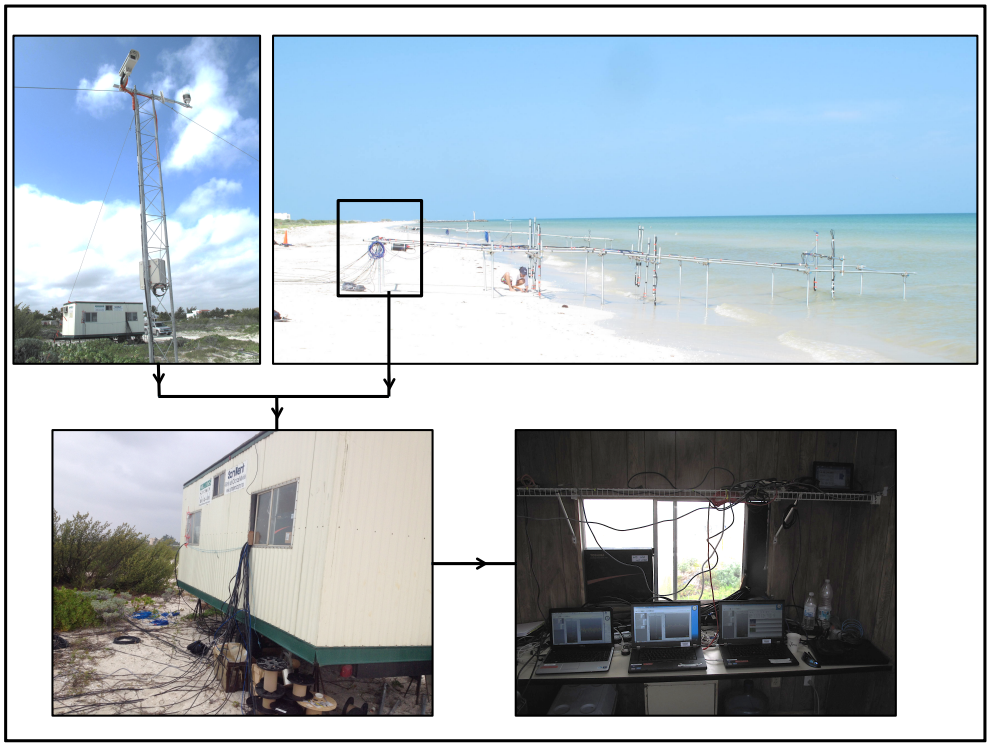

Figure 4. Measurement monitoring setup, (a) first transect (M1-M3) in the middle transect (b) camera and Visual-Met (c) monitoring station (d) real-time data monitoring system.

2.2. Morphology and sediment sampling measurement processes

Beach profiles were collected daily, except on the 5th and 8th of April. This was done using a totaling station, and Global Positional System (GPS), which provided position and elevation data. Figure 5 shows one of the team members taking beach profile measurements by totaling station.

Figure 5. A team member taking beach profile elevation measurement during the field experiment.

Foreshore sediment samples were collected on the left side of the frame (facing offshore on each transect). Prior to El-Norte (April 8th) and on the 10th of April, sediment samples were collected from M1-M6, E1-E5 and W1-W5 (See Figure 6-a). However, during El-Norte, sediment sampling was restricted to the frames on each transect (swash zone), due to the high wave activity which made it difficult to obtain samples from the surf zone. Since this study will only focus on the middle transect, only samples from M1-M6 were processed and analyzed. Figure 6-(b) shows the schematic of sampling during El-Norte for the middle transect. On the April 8th and 9th, sediment surface grab samples were collected next to each frame in addition to half step samples collected in between each frame span. From 15:00 April 8th to 06:00 April 9th an additional onshore sampling location was added to account for the high swash events that occurred during

the storm. During the end of the storm (08:00-10:00 April 9th) sampling was decreased (collected just next to each frame span).

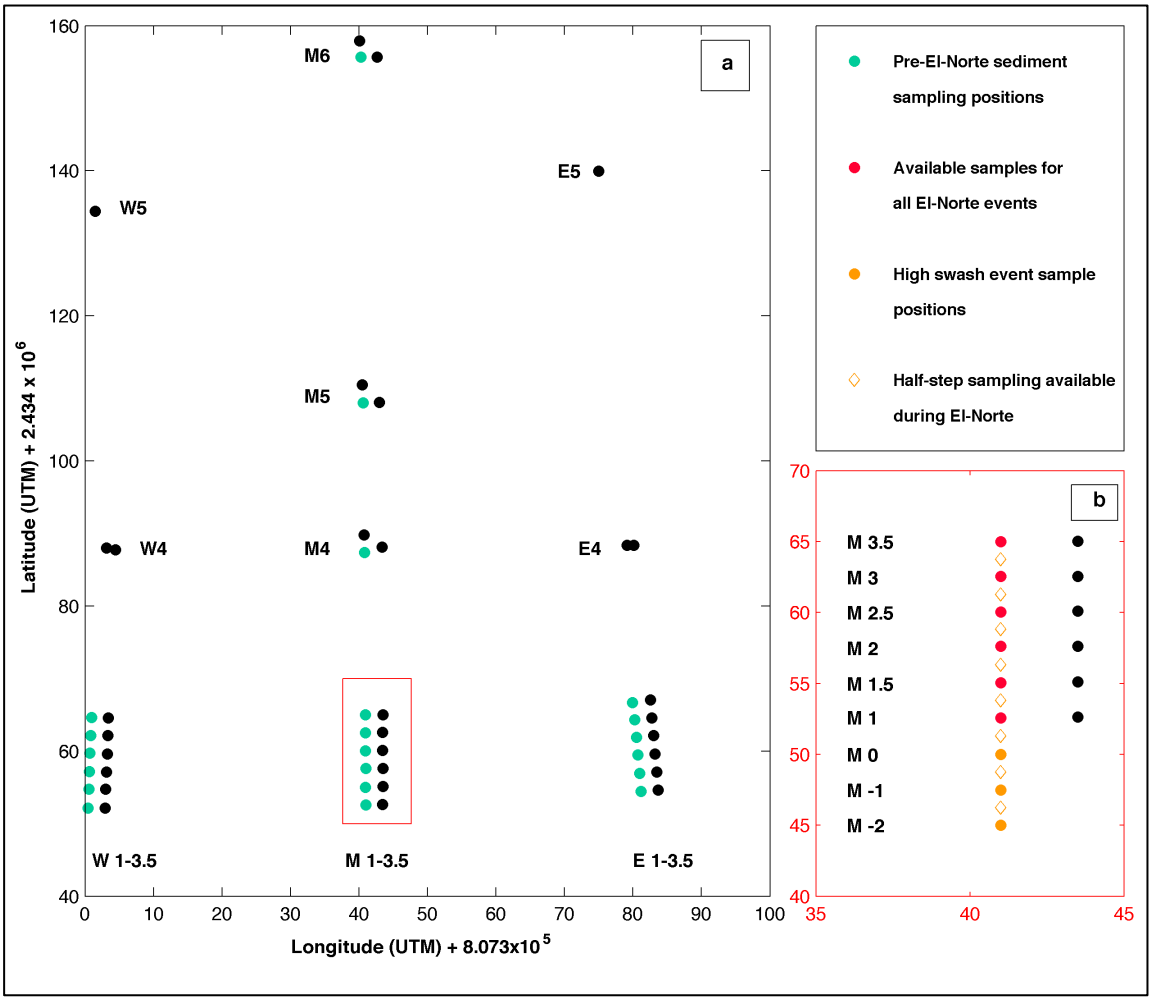

Figure 6. Locations of vertical frame shoring posts and sediment sampling locations. Sediment grab samples were collected daily (panel a). During El-Norte sediment sampling frequency in time and space were increased (panel b), each circle in the figure represents the location of a vertical shoring post but only the colored (green, red, and orange) locations were used as sampling locations.

2.2.1. Sediment processing

Sediment grain size distributions were obtained using two methods based on the size of the particles, which are: 1) traditional sieve analyses and 2) particle laser diffraction. For the sieve analyses, samples were manually sieved for particle sizes greater than 1.18 mm. Laser diffraction was used to measure the grain size distribution of grains less than 1.18 mm using a Malvern Mastersizer 2000®. The Mastersizer can measure grain sizes between 2×10^{-5} mm and 2 mm by detecting scattered light from suspended particles. The instrument computes an average of three results and outputs the grain size distribution in an ASCII-File. Well-mixed fractions of 5 g of pre-sieved samples were inserted into the Mastersizer. The Mastersizer computes grain sizes based on volume whereas sieve analysis gives sizes fractions by weight. Therefore in order to obtain continuous grain size distribution curves both where merged by averaging points between the minimum sieve analysis value and highest value from the Mastersizer, and the sieve analysis values were presented as mean grain size between adjacent sieves rather than sieve sizes to better match the Mastersizer results. In addition, it was assumed that all particles had the same density and the percent by volume will equal percent by weight. Total mass (M_{total}) was calculated assuming constant particle density as:

$$M_{total}=\frac{m_{retained}}{m_{total}}\times100 \quad (1)$$

where M_{total} is a percentage by weight; $m_{retained}$ is the mass of sediment retained (g) on the sieve; and m_{total} is the total mass of the sample (g).

Using the data obtained from manual sieving and the Mastersizer, statistical calculations were performed to obtain the median sediment diameter (d_{50}) in mm. d_{50} can be obtained from the cumulative distribution curve with 50% of the sediment sizes in the sample being coarser and 50% being finer by weight. 68% of all sediment sizes are $\pm$ one standard deviation from the mean diameter. *Dean and Dalrymple* [2002] suggested that mean diameter should be calculated in phi scale (ϕ) using the method proposed by *Otto* [1939] and *Inman* [1952], where ϕ_{84} and ϕ_{16} are important in describing sediment:

$$M_{d\phi} = \frac{(\phi_{84} + \phi_{16})}{2} \tag{2}$$

where $M_{d\phi}$ is the mean diameter, and ϕ_{84} coarser and ϕ_{16} coarser are percentages by weight of the cumulative distribution in phi units. A numerical measurement of sorting was obtained using the standard deviation (σ_ϕ):

$$\sigma_\phi = \frac{(\phi_{84} - \phi_{16})}{2} \tag{3}$$

Another measurement that is commonly used to describe the distribution of sediment is skewenss (α_ϕ):

$$\alpha_{\phi} = \frac{M_{d\phi} - \phi_{50}}{\sigma_{\phi}} \quad (4)$$

where negative values of α_{ϕ} represent an erosional environment, as the finer sediment have been removed due waves and currents, whereas a positive values indicate a depositional environment [*Dean and Dalrymple*, 2002].

Sediment grain size was converted from mm to phi (ϕ) using equation (5), however, after the calculations values of d_{50} have been converted back by using equation (6):

$$\phi = -\log D_{(mm)} \quad (5)$$

$$D_{(mm)} = 2^{-\phi} \quad (6)$$

2.3. Hydrodynamic measurements processing and calculations

2.3.1. Significant wave height and wave period

Wave height (H) and period (T) were calculated using the zero-upcrossing method from surface elevation data measured by the three PTs (swash zone and inner surf zone) and three ADVs internal pressure sensors (surf zone). Both the measurements obtained from the ADVs and the PTs were continuous. Prior to data analysis the raw data have been converted to burst of 5 minutes in order to obtain the wave processes and make the analysis less time consuming instead of dealing with very large data sets.

The measurements obtained from PTs had some errors produced by readings taken while the sensors were exposed to air (mainly during low tide). Any measurements taken out of the water were replaced by Not A Number (NaN) values prior to wave

analysis. The surge level was obtained by the difference between the predicted and observed tide.

Wave heights were calculated using the zero-upcrossing method which finds two adjacent zero-upcrossing points in the wave time series and estimates H as the vertical distance between the highest and lowest surface elevation between the two zero-upcrossings. The associated wave period is the time between the two zero-upcrossing points. Figure 7 demonstrates the zero-upcrossing method (e.g. *Pierson* [1954]). The mean zero crossing wave height ($\overline{H}$) can be calculated using equation (7):

$$\overline{H} = \frac{1}{N}\sum_{i=1}^{N} H_i \tag{7}$$

where i represents the number of the waves processed, and N is the total number of waves.

The mean zero-upcrossing period ($\overline{T}$) was calculated using equation (8)

$$\overline{T} = \frac{1}{N}\sum_{i=1}^{N} T_i \tag{8}$$

where i represents the number of the waves processed, and N is the total number of the waves. Significant Wave Height (H_s) which is the mean of the largest one third of the waves has been calculated using equation (9), where j represents ranked wave height (highest to lowest):

$$H_s = \frac{1}{\frac{N}{3}} \sum_{j=1}^{\frac{N}{3}} H_j \tag{9}$$

Wave Period (T_s) has been calculated using equation (10):

$$T_s = \frac{1}{\frac{N}{3}} \sum_{j=1}^{\frac{N}{3}} T_j \tag{10}$$

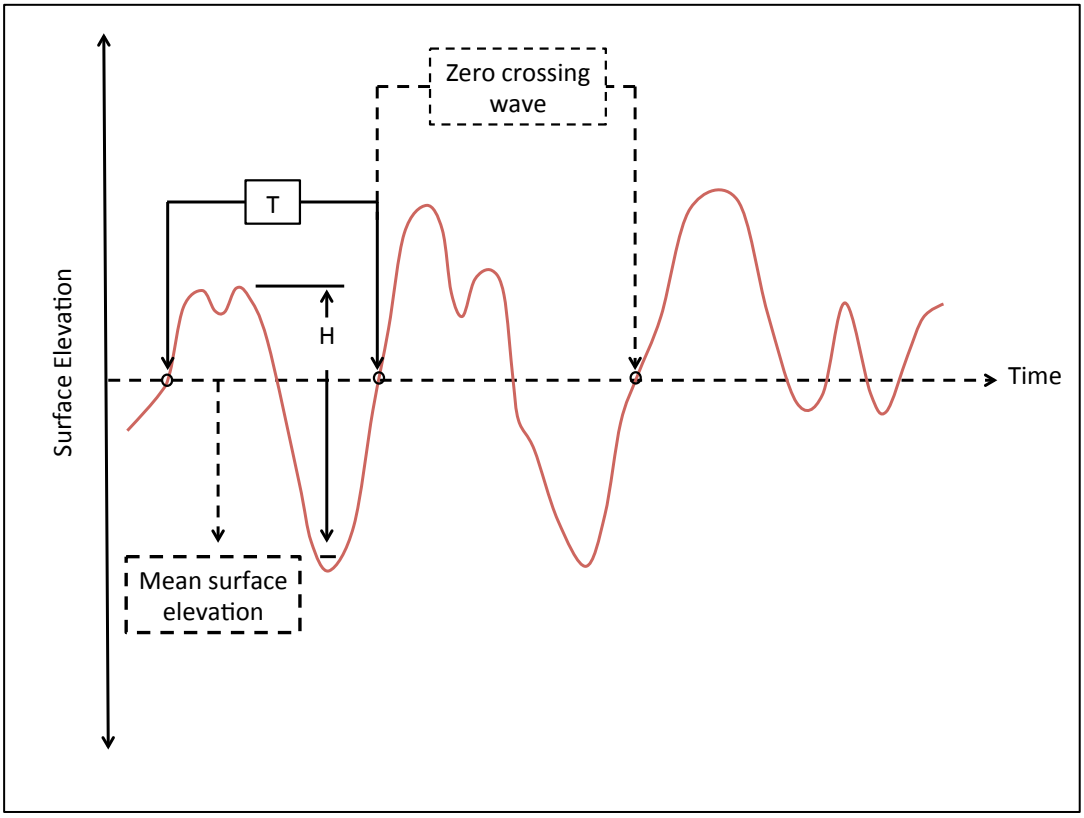

Figure 7. Estimating wave height and wave period using the zero-upcrossing method (adopted from *Sorensen* [1993]).

2.3.2. Cross/longshore velocity, shear stress, turbulent kinetic energy and turbulent kinetic energy dissipation calculations

Eulerian velocity measurements, within the surf zone, were collected using 3 ADVs located at M4, M5, and M6. After selecting the time frames to be studied in this paper a 5-minute moving average velocity was calculated, which resulted in smoother, de-spiked data.

Bottom shear stress (τ_b), turbulent kinetic energy (TKE) and turbulent kinetic energy dissipation (ε) were estimated using the ADVs velocity time series. Prior to analyzing, any results found with correlation less than 70% were converted to NaN as recommended by the manufacturing company Nortek. Velocity time series were portioned into 4096 sample blocks prior to analysis to avoid complications from having to handle large files. TKE was computed using the "variance" method, which uses the velocity fluctuation as shown in equation (11):

$$TKE = \frac{1}{2}\left(\overline{u'^2} + \overline{v'^2} + \overline{w'^2}\right) \tag{11}$$

where $\overline{u'^2}$, $\overline{v'^2}$, and $\overline{w'^2}$ are east-west, north-south and vertical mean velocity variances (e.g. *Rippeth et al.* [2003]). This approach depends on the difference velocity ($u, v,$ and w) on the ADV beams. In addition, it is assumed that the water column is well-mixed and horizontally uniform.

In addition, ε was estimated using equation (12) :

$$\varepsilon = \frac{u_*^3}{kz} \tag{12}$$

where u_* is the frictional velocity ($u_* = \overline{u'w'} = C_d\overline{|u|^2}$). C_d is the nondimensional drag coefficient which equals 10^{-3}, κ is the empirical von Kármán constant ($\kappa = 0.41$) and z is the distance above the bed (for details see *Feddersen* [2012] and *Feddersen et al.* [2007]).

Finally, bed shear stress τ_b was estimated using the covariance method, which uses the velocity fluctuation in the mean direction of flow and the vertical direction of the mean flow velocity, as shown in equation (13):

$$\tau_b = \rho\,(\varepsilon kz)^{\frac{2}{3}} = \rho\,\overline{u'w'} \tag{13}$$

where ρ is the density of the salt water and is assumed to be constant (1025 kgL^{-1}). This method can be used with instruments that record high precision velocity measurements such as ADV (e.g. *Babaeyan-Koopaei et al.* [2002]; *Biron et al.* [2004]; *Kim et al.* [2000]; *Pope et al.* [2006]; *Rippeth et al.* [2003] and *Williams and Simpson* [2004]).

3. RESULTS

3.1. Meteorological observations

Wind observations during the study period revealed the presence of diurnal sea/land-breeze systems and one El-Norte event that started midday of April the 7th and ended midday of April the 9th (Figure 9). These atmospheric processes were correlated with diurnal variations of temperature and humidity, and the effect of El-Norte was significant, leading to a clear and distinguishable decrease in temperature and humidity, and an increase in atmospheric pressure and wind speed (Figure 8 panels a, b and c, Figure 9 Panel b). Wind stress (τ_w) was computed using equation (14) in order to observe the effect of wind stress magnitude on the waves within the surf zone.

$$\tau_w = C_D \rho U_h^2 \tag{14}$$

C_D is the drag coefficient estimated using the method proposed by *Smith* [1988], ρ is air density assumed to be constant (1.2 Kgm^{-2}) and U_h^2 is wind speed squared at a reference height (10 m). It can be seen in Figure 9 (b) that the maximum wind speed during LB was 6.5 ms^{-1}, 11 ms^{-1} during SB, and 14.5 ms^{-1} during El-Norte. There was a significant change in wind speed between LB and SB, however during El-Norte the wind dramatically increased in the first hours followed by a linear decrease. The wind magnitude in Figure 9 (panel c) shows abrupt change in wind direction between LB and SB (from SW to NE). Conversely, a continuous northerly wind was observed during El-

Norte. The magnitude of τ_w showed a significant increase during El-Norte, reaching a peak of 0.58 Nm^{-2} in comparison to SB and LB that had lower values of τ_w (Table 1).

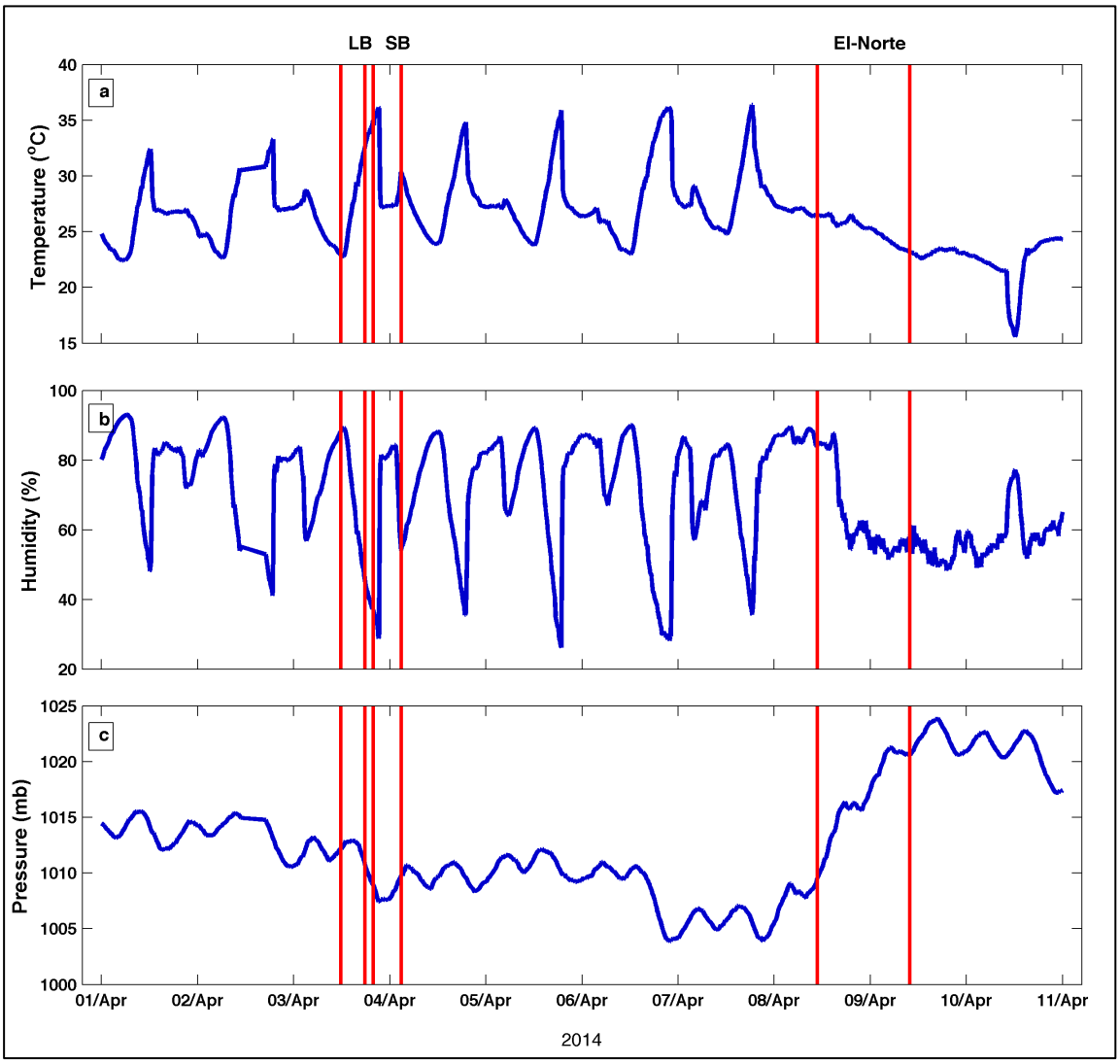

Figure 8. Meteorological observations obtained from Visual-Met (a) temperature measurements (b) humidity measurements and (c) atmospheric pressure.

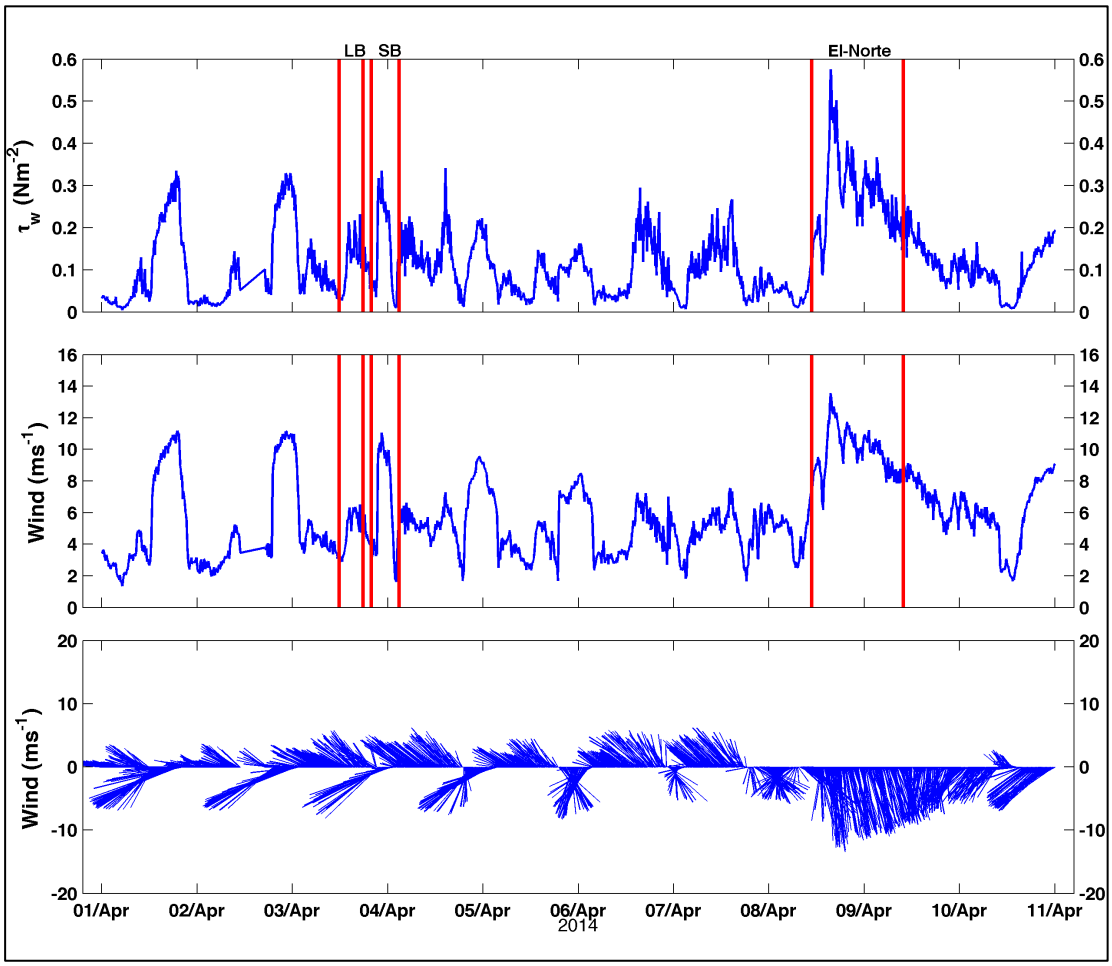

Figure 9. Wind observation from April 1st to April 11th, where (a) estimated τ_w (b) measured wind speed (c) wind speed and direction. Arrows pointing up indicate southerly winds, while downward arrows indicate northerly winds.

Table 1. Basic statistics for computed wind stress and average wind direction.

	Mean wind stress (τ)		
Event	Magnitude (Nm^{-2})	Maximum (Nm^{-2})	Direction (degrees)
LB	0.12	0.23	138.3
SB	0.15	0.34	87.7
EL-Norte	0.28	0.58	341.97

It can be seen from the wind-rose (Figure 10), that, the dominant wind was northerly (mainly northwesterly winds) during the whole measurement period, in addition to easterly and southeasterly winds (these winds were strong with an average of 10 ms^{-1}). However, there was insignificant measurement recorded between south-south-east to north-west-north directions, which may be as a result of the anemometer being blocked leading to an underestimated measured wind magnitude during LB.

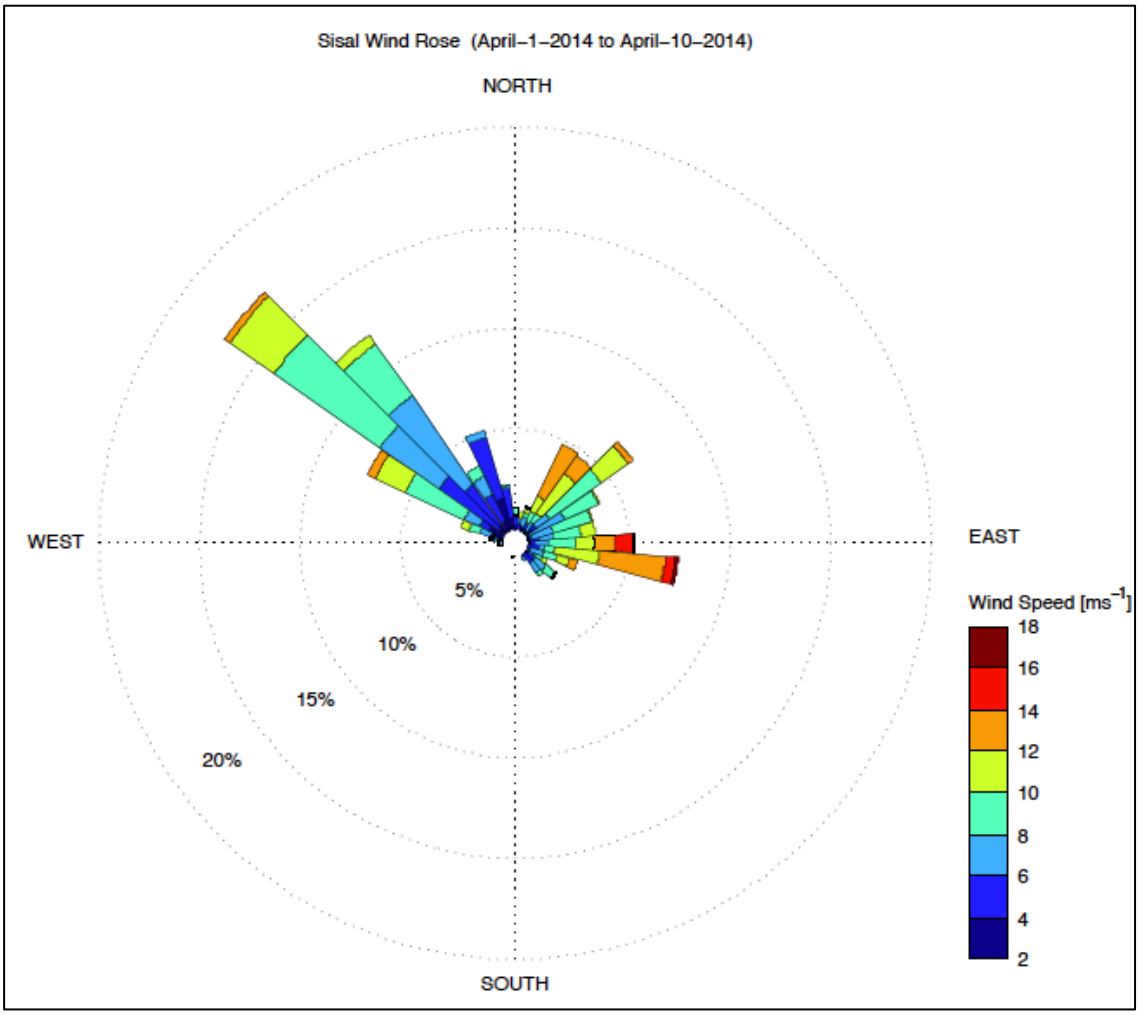

Figure 10. Wind rose plot (wind speed and direction) for the measurement time period (1^{st}-10^{th} April 2014).

3.2. Sediment analysis

3.2.1. Grain size distribution and classes

Sediment distributions at M1 for LB and SB were almost the same, with 84% of fine sand during LB and 88% during SB. The majority of the sediment was found to be in the fine and medium sand-size fraction during both events (Figure 11). However, El-Norte caused significant changes to the distribution with variations in the fine and medium sand fractions. The most significant change occurred on the 8th at 11:00, where sediment shifted to a coarser fraction, with more medium sand and fine gravel. Near the end of the El-Norte storm the distribution became similar to the SB distribution curve. On the other hand, medium sand fraction was observed more at M2 than M1, while coarser sand and fine gravel were found in the middle period of El-Norte. The finer sand was found at M3 for both LB, SB, and during the 9th of April. LB and SB were almost the same for the distribution curve at M3, however SB was observed to have less fine sand. During the beginning of El-Norte the distribution shifted more towards fine sand (between 80% and 90%) while at the end of the storm it reached 10%.

Figure 12 shows the distribution of sediment for LB and SB events only. Having compared all the positions (M4, M5, and M6) it can be noticed that they were very similar. At position M4 during both LB and SB approximately 91% of fine sand and 8% of medium sand was observed, while the rest was found to consist of coarse sand. M5 had almost 100% fine sand, where M6 had approximately 100% fine sand for LB and 96% fine sand for SB. More coarse sand was found during SB compared to LB at the M6 location.

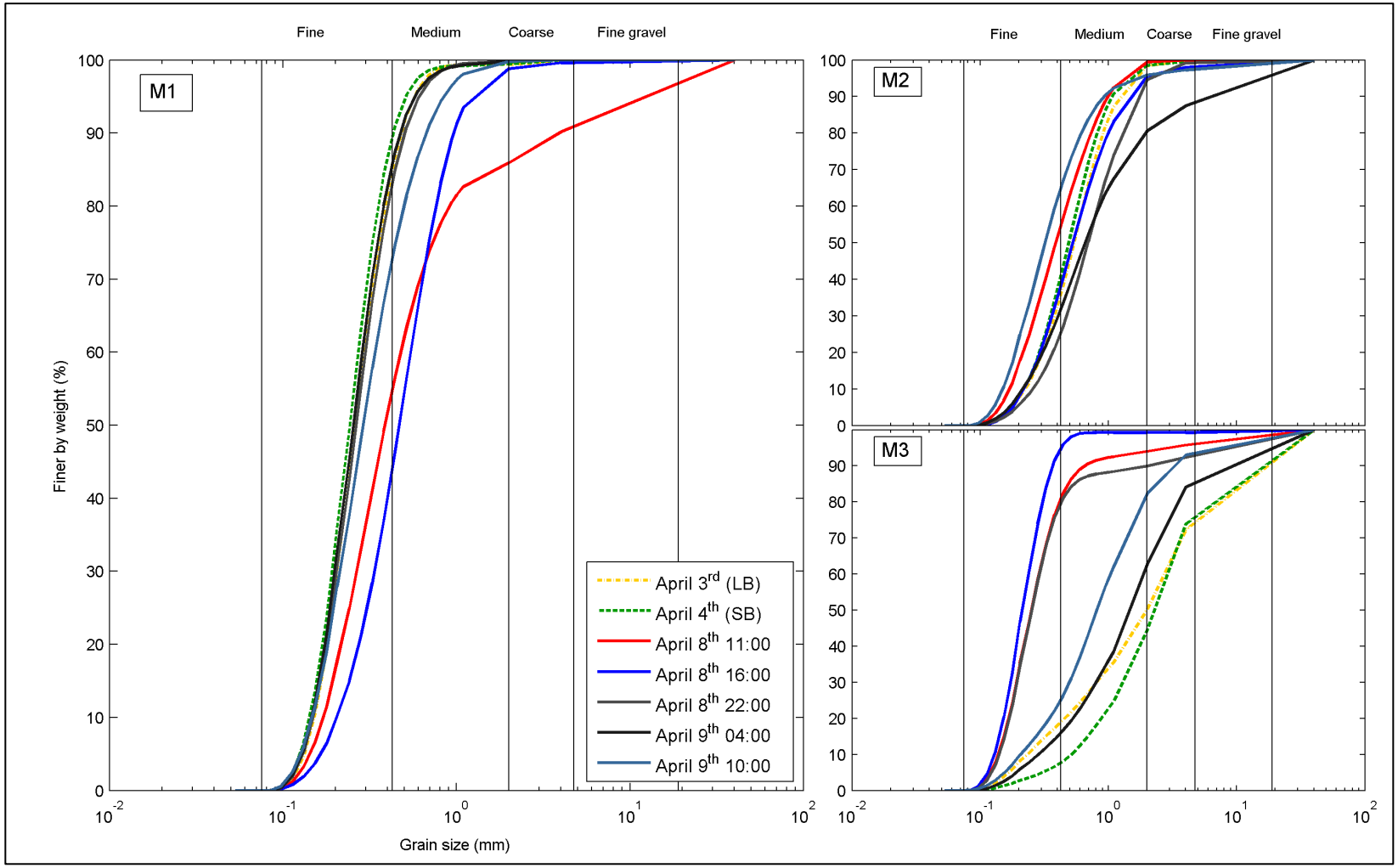

Figure 11. Grain size distribution at M1, M2 and M3 locations for SB, LB and El-Norte.

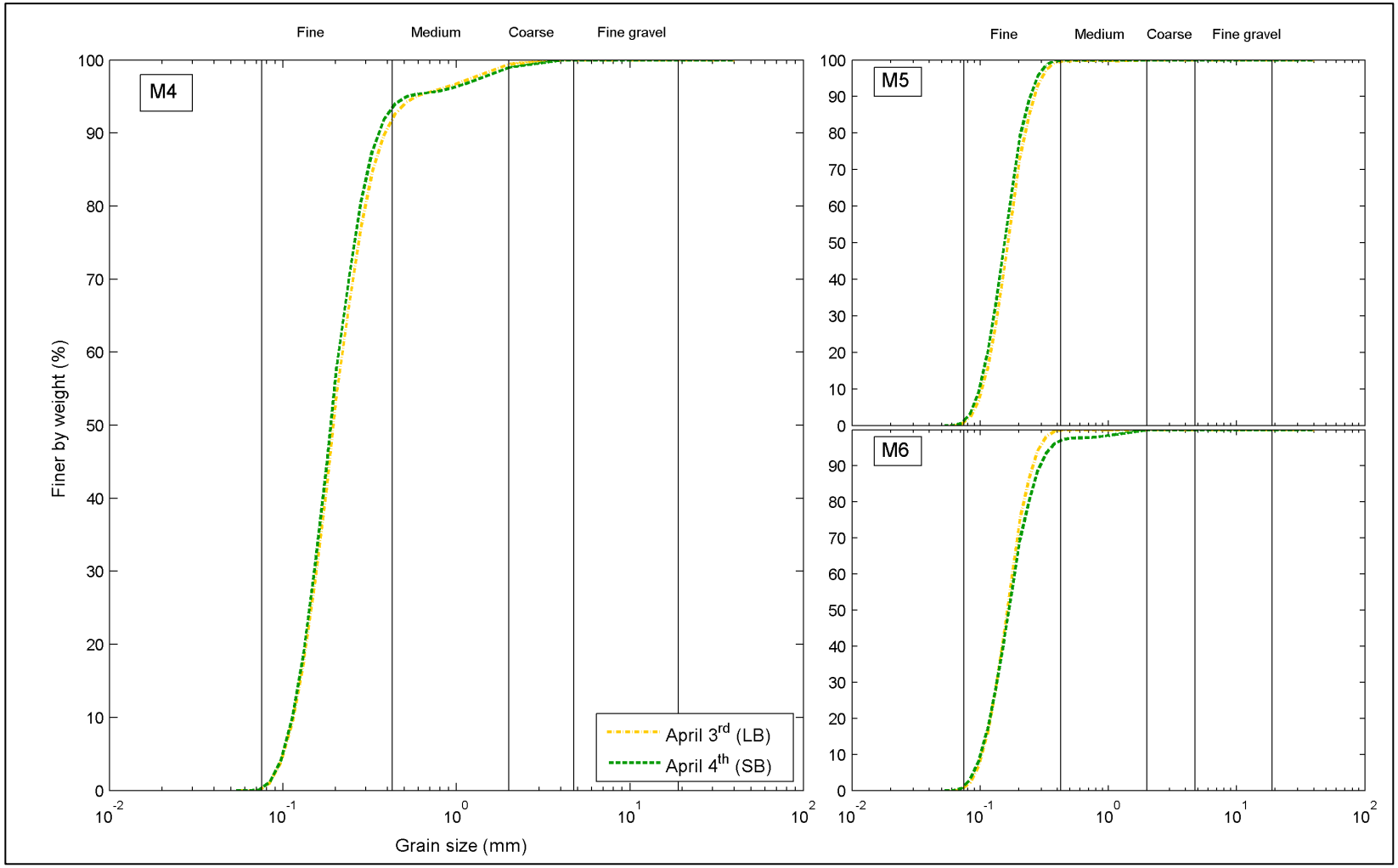

Figure 12. Grain size distribution at M4, M5 and M6 locations for SB, LB.

Another method to present the relative change in the sediment distribution along the cross-shore in percent by weight is shown in both Figures 13 and 14. Figure 13 illustrates a comparison of grain classes between LB and SB. It can be noticed that both, LB and SB events, had nearly the same grain class pattern for all positions. Fine sand was dominant at position M1, however M2 had a higher percentage of medium sand. During LB M3 had a similar percentage by weight, but SB had 10% less fine sand than LB. The highest percentages of fine sand were found at locations M4, M5 and M6. The highest percentage of fine sand was found at M5, however it had a lower percentage of medium sand and an insignificant percentage of coarse sand and fine gravel.

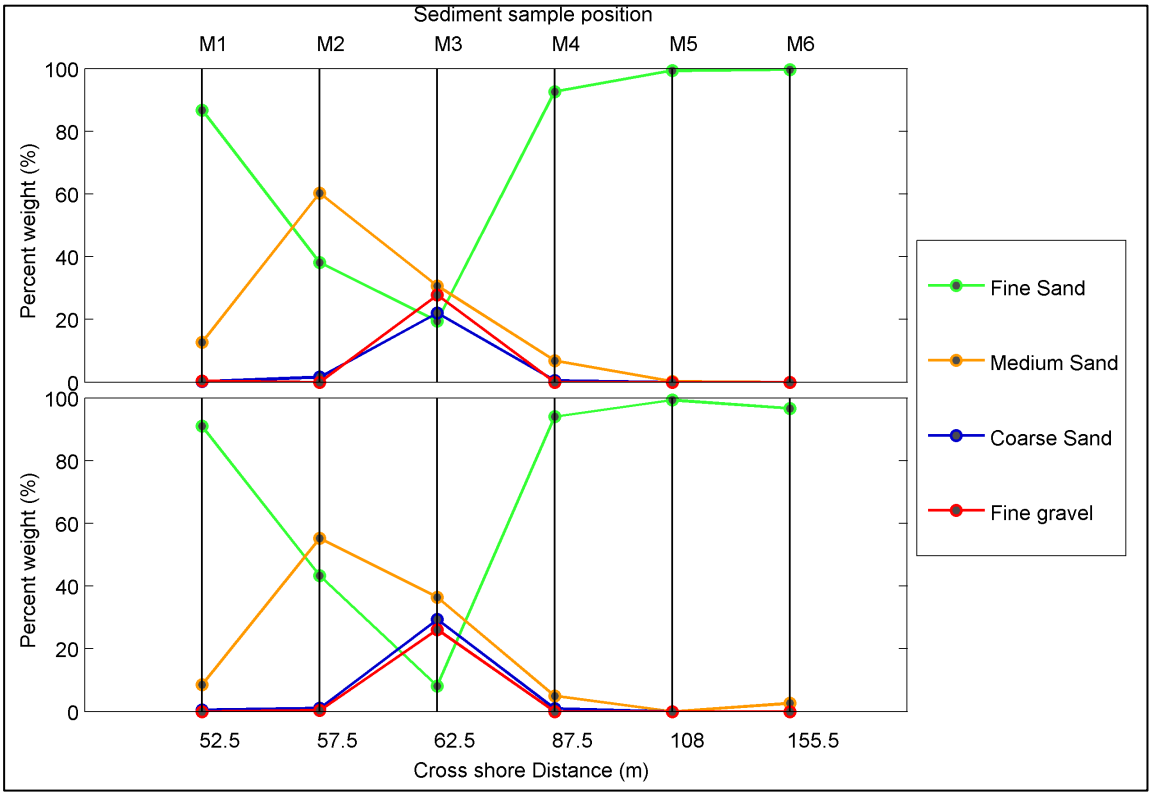

Figure 13. SB and LB grain class variations for positions from M1 to M6.

It can be observed from Figure 14 (panel a, b, c, d, and e) that position M3 had less coarse sand and fine gravel than the percentages observed during LB and SB in Figure 13. In addition, M1 showed an increase of fine sand, and overall a decrease in medium sand except in panels (d) and (e). High temporal variability in percentage by weight was observed at location M3, with a high percentage of sand found in panels (a) and (b), followed by a decrease (panels c, d, and e). Medium, coarse sand, and fine gravel were decreasing at the beginning of El-Norte, but an increase was noticed on the 9th as shown in panels (d) and (e).

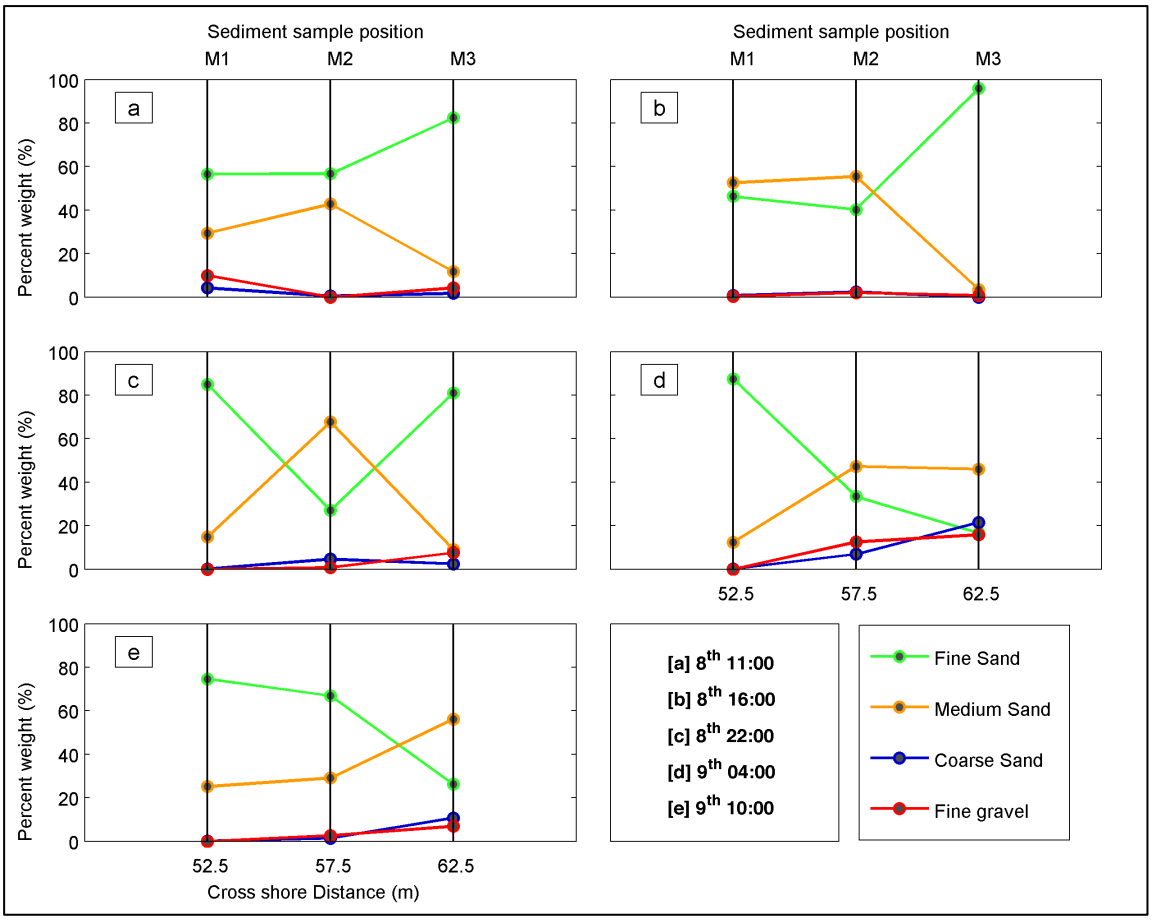

Figure 14. El-Norte grain class variations for positions M1 to M3.

3.2.2. Cross-shore beach profile observation

Figure 15 shows the cross-shore beach profile survey for the 3rd, 4th, 7th (pre-El-Norte), and the 9th (2nd day post-El-Norte). It can be observe that on the 3rd the beach profile had a step at 53 m, and two sandbars at 97 m (-1.2 m) and 160 m (-1.45 m). Approximately 0.15 m retreat of the beach step was observed during SB, and a migration of the first sandbar landward (94m and seabed -1.1m). Noticeable erosion of the trough was also observed between the first and the second sandbar.

Furthermore, the pre-El-Norte beach profile indicates slight erosion at M1 and M3, while deposition of sediment in the surf zone was noticed. The deposition was high between 90 m and 185 m offshore, as the first sandbar showed vertical growth of 0.4 m compared to the LB profile. In addition, a sandbar was created in the trough between M5 and M6 that had a maximum increase in elevation (0.34 m) compared to the other events. A significant change of the beach profile was observed during El-Norte, where the beach slope became 1.5^{o} steeper (between 46 m and 58 m), but a decrease of 0.7^{o} between 60 m and 65 m was noted to make that section shallower. Moreover, deposition of sediment was observed between 47 m and 63 m, and the migration of the beach step approximately 7 m seaward. The most noticeable change that can be seen by comparing changes between pre and post El-Norte beach profiles was the erosion within the surf zone especially within the trough and the second sandbar. Erosion of 0.44 m was observed from 155 m to 160 m. In addition, a decrease in height of 0.6 m was observed on the second sandbar.

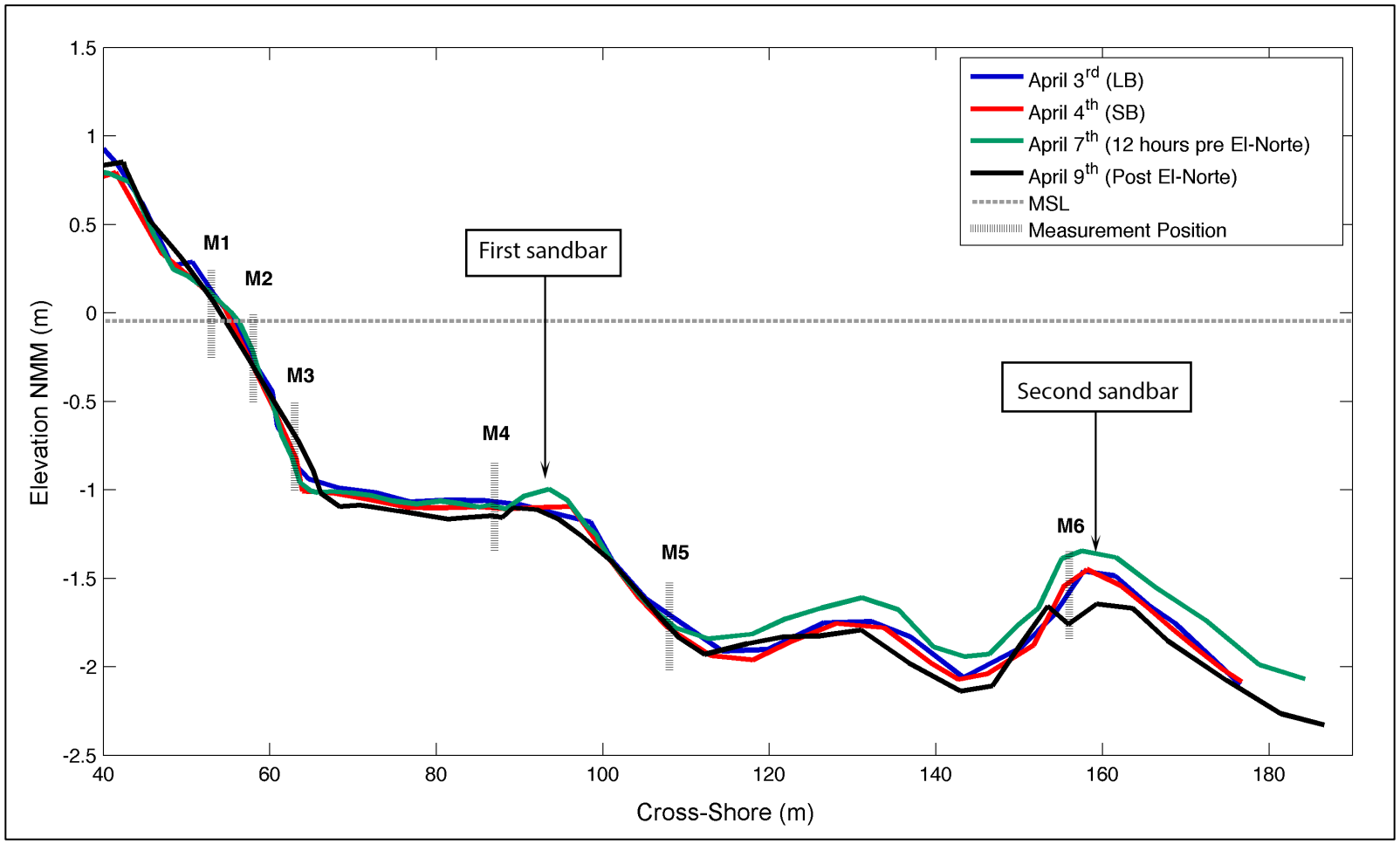

Figure 15. Measured cross-shore beach profiles for the 3rd, 4th, 7th (pre El-Norte) and the 9th (post El-Norte), where y axis represent measurements from *Nivel Medio del Mar* (NMM) i.e. mean tidal level, and cross-shore 0m represent the field station.

3.3. Hydrodynamics analysis

3.3.1. Swash zone and surf zone waves observation

Estimated H_s and T_s of breaking waves obtained from the PTs located at M2 and M3 can be seen from figures 16, and 17, while Figures 18, 19, and 20 show the results obtained from the ADV's pressure sensors located at M4, M5, and M6, respectively. Panel (a) in all figures mentioned above shows the variation in H_s and T_s from 1st to the 11th of April; while LB results can be seen from panel (b), in addition to panel (c) showing SB results and panel (d) represents El-Norte results.

Prior to El-Norte the maximum H_s and T_s were found to be associated with SB. H_s showed a similar pattern as the wind speed and τ_w, which suggests that coastal region is dominated by wind waves. The maximum H_s (broken and/or swash waves) for LB, SB and El-Norte at M2 were 0.16 m, 0.26 m and 0.35 m, respectively, while at M3 (located at the surf zone) the maximum was 0.16m, 0.25m and 0.42m. Both Figures 20 and 21 show almost the same results where H_s and T_s increase during strong wind events. However, waves at location M3 were found to be higher than the ones at M2. Figures 18, 19, and 20 show a similar result to the observation at M2 and M3 in terms of each event's effect on H_s and T_s. However, the estimated results of H_s and T_s were higher. It can also be seen from the results obtained from the ADVs that H_s and T_s were decreasing landward. Mean and maximum values of estimated H_s and T_s were computed and are shown in Tables 2 and 3.

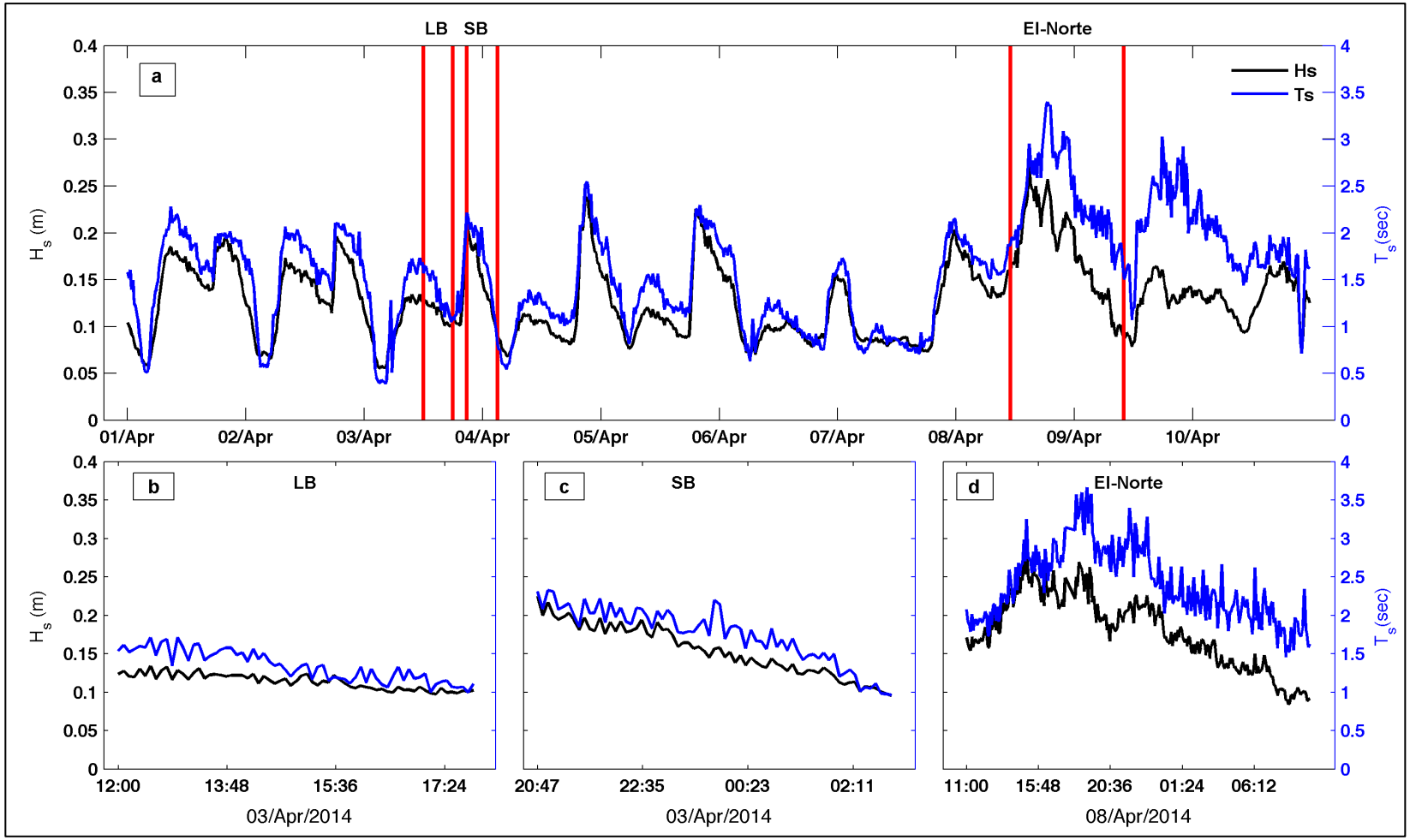

Figure 16. H_s and T_s analysis for M2 (a) 15 minutes average H_s and T_s from April 1st to April 11th (b) 5 minute average H_s and T_s for LB (c) 5 minute average H_s and T_s for SB (d) 5 minute average H_s and T_s for El-Norte.

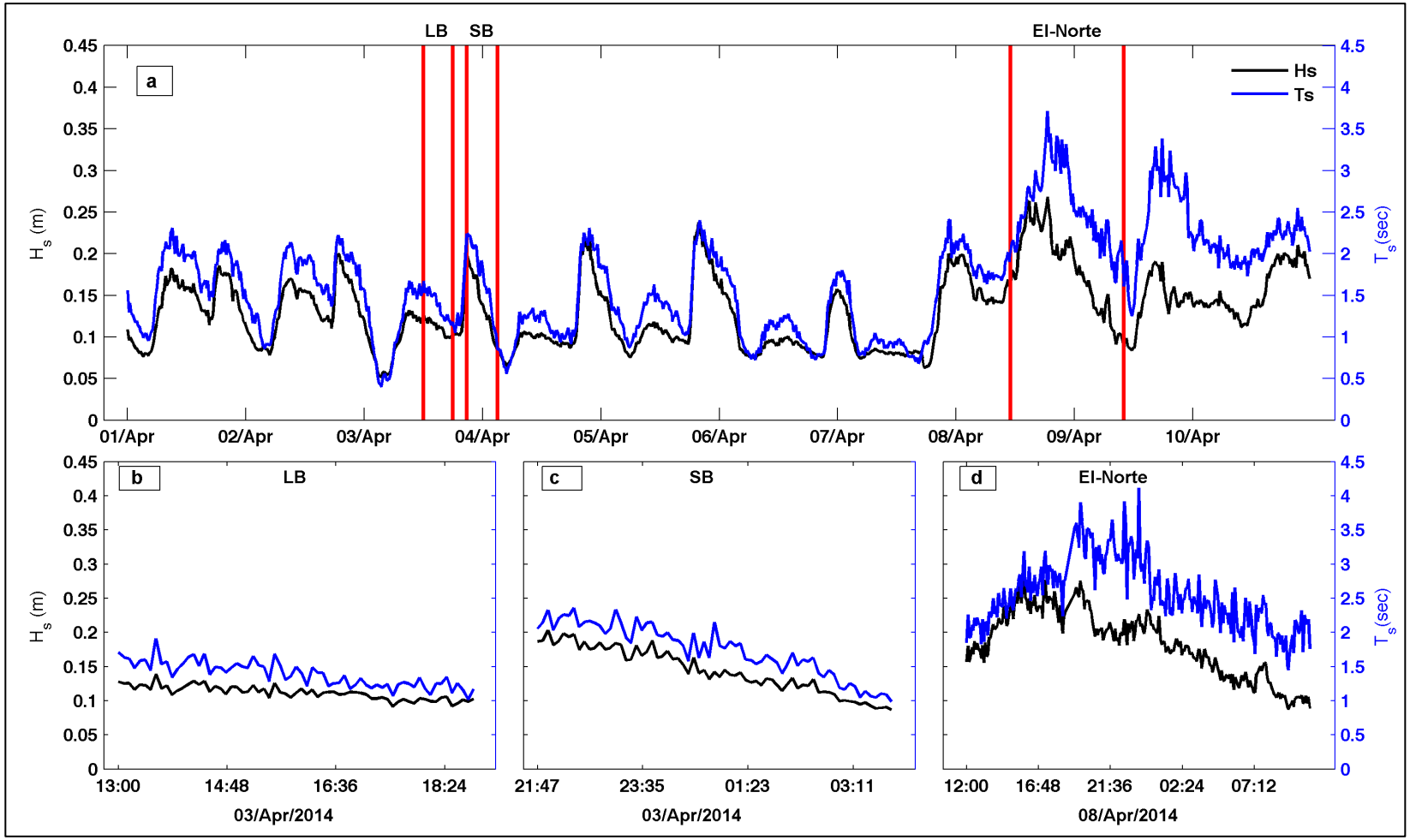

Figure 17. H_s and T_s analysis for M3 (a) 15 minutes average H_s and T_s from April 1st to April 11th (b) 5 minute average H_s and T_s for LB (c) 5 minute average H_s and T_s for SB (d) 5 minute average H_s and T_s for El-Norte.

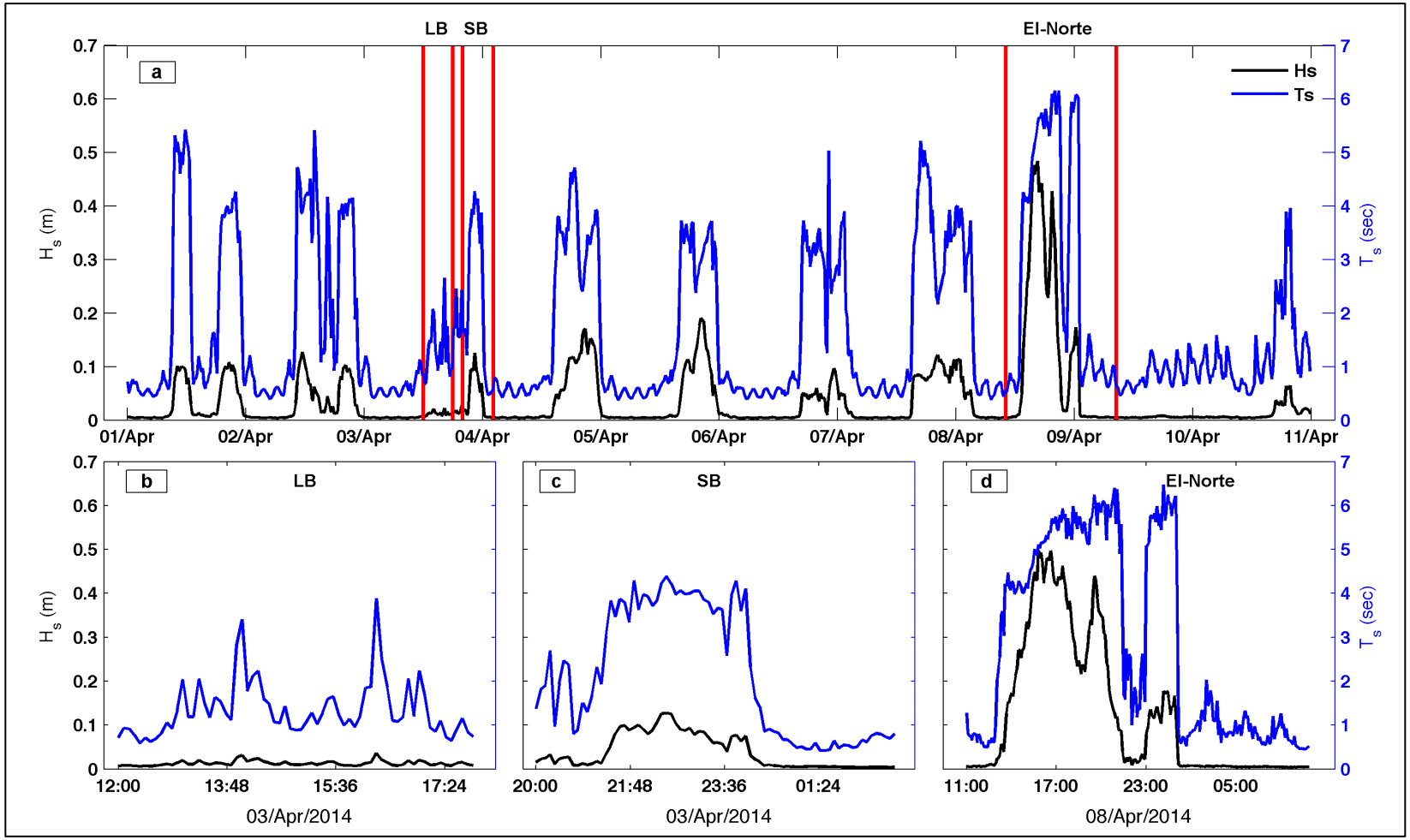

Figure 18. H_s and T_s analysis for M4 (a) 15 minutes average H_s and T_s from April 1st to April 11th (b) 5 minute average H_s and T_s for LB (c) 5 minute average H_s and T_s for SB (d) 5 minute average H_s and T_s for El-Norte.

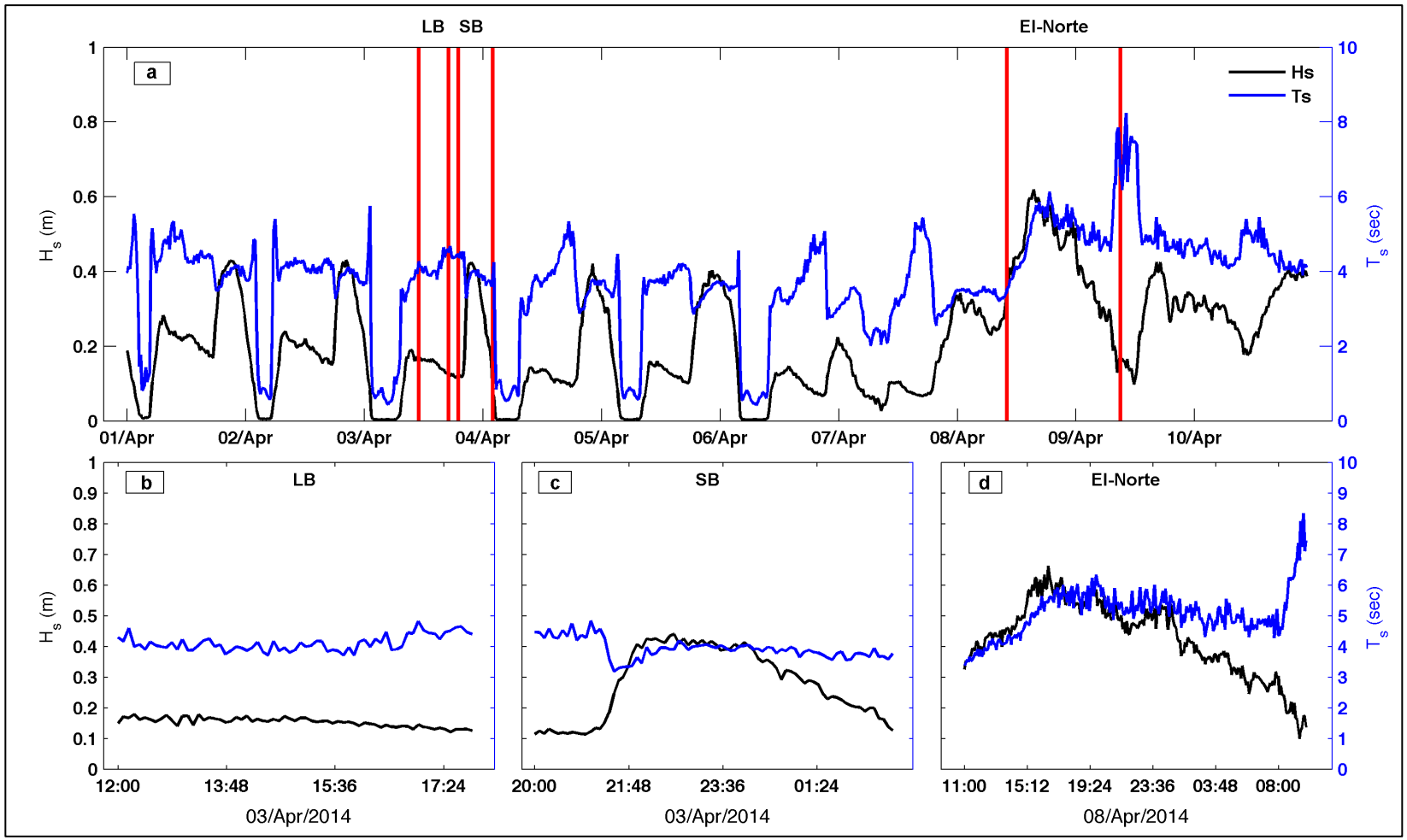

Figure 19. H_s and T_s analysis for M5 (a) 15 minutes average H_s and T_s from April 1st to April 11th (b) 5 minute average H_s and T_s for LB (c) 5 minute average H_s and T_s for SB (d) 5 minute average H_s and T_s for El-Norte.

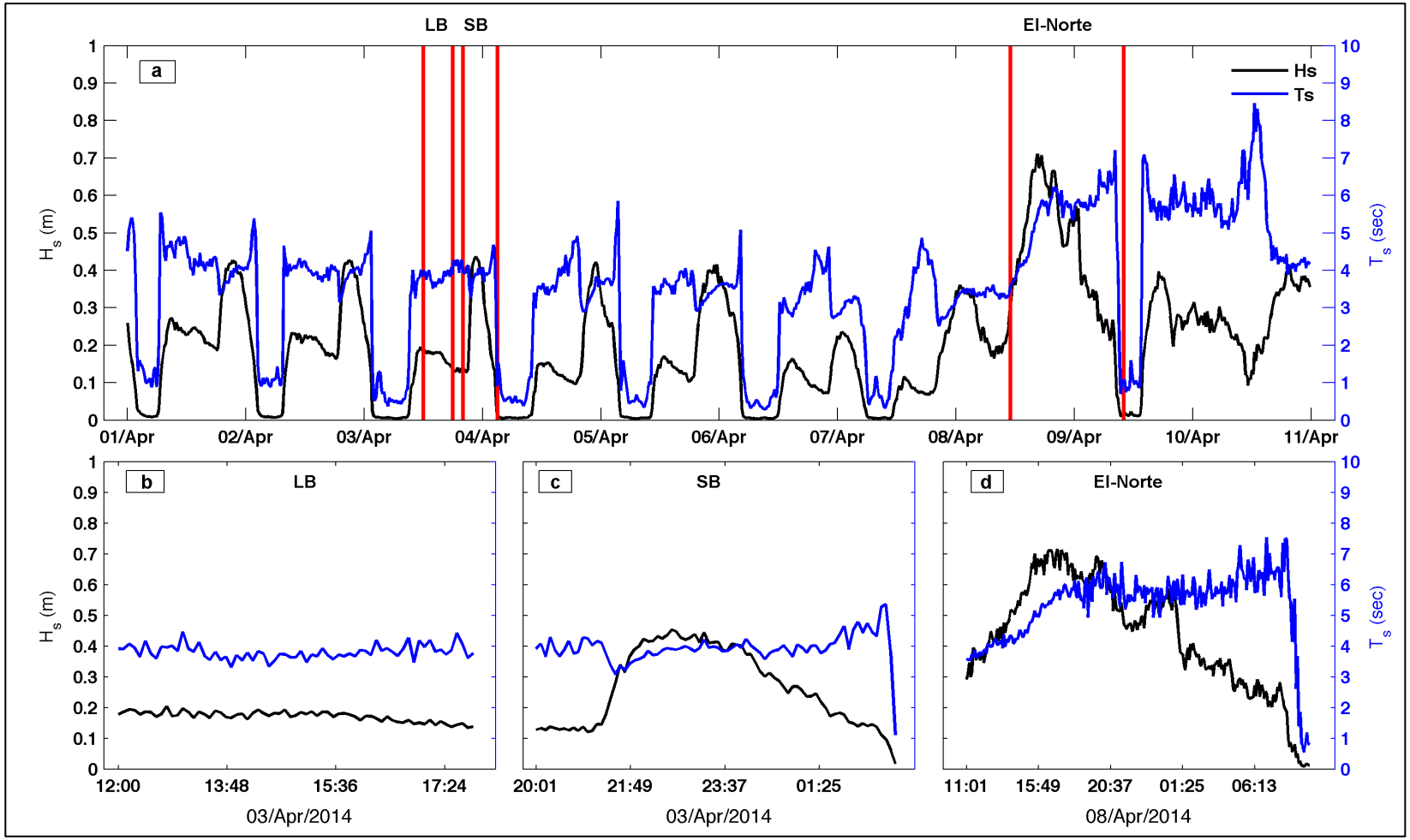

Figure 20. H_s and T_s analysis for M6 (a) 15 minutes average H_s and T_s from April 1st to April 11th (b) 5 minute average H_s and T_s for LB (c) 5 minute average H_s and T_s for SB (d) 5 minute average H_s and T_s for El-Norte.

Table 2. Basic statistics for computed H_s for LB, SB, and El-Norte at each position.

	H_s statistics							
	Mean H_s (m)				Max H_s (m)			
Position	LB	SB	El-Norte	Overall	LB	SB	El-Norte	Overall
M2	0.11	0.15	0.18	0.13	0.13	0.22	0.31	0.28
M3	0.11	0.14	0.18	0.13	0.14	0.2	0.29	0.27
M4	0.01	0.04	0.12	0.04	0.04	0.13	0.5	0.48
M5	0.15	0.28	0.43	0.21	0.18	0.44	0.66	0.62
M6	0.17	0.27	0.44	0.20	0.20	0.45	0.72	0.71

Table 3. Basic statistics for computed T_s for LB, SB, and El-Norte at each position.

	T_s statistics							
	Mean T_s (sec)				Max T_s (sec)			
Position	LB	SB	El-Norte	Overall	LB	SB	El-Norte	Overall
M2	1.34	1.75	2.38	1.58	1.71	2.33	3.67	3.4
M3	1.39	1.75	2.55	1.66	1.91	2.36	4.12	3.72
M4	1.35	2.16	2.92	1.7	3.88	4.39	6.47	6.16
M5	4.11	3.93	5.09	3.76	4.82	4.84	8.34	8.24
M6	3.81	3.93	5.32	3.56	4.47	5.36	7.54	8.46

3.3.2. Surf zone longshore/cross-shore current

The observations obtained from the ADV positioned at M4 (located in approximately 1 m water depth with the sensor head 0.15 m above the bed) showed a constant onshore and eastward current direction during the SB events, in addition to an increase in current velocity (Figure 21 panel a). On the other hand, during LB the cross-shore current direction was found to be offshore, while the longshore current varied between eastward and westward. However, it can be noted that the cross-shore current velocity decreased significantly at the end of SB's events on average of 0.35 ms^{-1}. During the chosen LB event (Figure 21 (b)) it was found that both longshore and cross-shore current velocities were relatively low with a maximum velocity of 0.05 ms^{-1}. The direction was found to be mainly onshore and eastward. Furthermore, high onshore current velocities of 0.58 ms^{-1} and eastward current with a mean velocity of 0.27ms^{-1} were observed during SB (Figure 21 panel c). It can be seen that during pre-El-Norte the current shifted towards offshore and eastward directions while post-EL-Norte the cross-shore current increased and shifted to offshore and long-shore current shifted to eastward with velocities of 0.4 ms^{-1} and 0.8 ms^{-1}, respectively (Figure 21 panel d).

Figure 22 shows the results obtained from the ADV positioned at M5, where it can be seen that the main direction of the current from the 1st to the 7th of April was mainly onshore and westward. However, SB events resulted in higher current velocity, when compared to LB events (Figure 22 (a)). Figure 22 (b) shows the current velocity and direction during LB, where both longshore and cross-shore currents found to be onshore and westward directed with an average longshore velocity of 0.02 ms^{-1} and

0.034 ms^{-1} cross-shore. On the other hand, a clear increase in the longshore current velocity was observed during SB and El-Norte with a maximum of 0.14 ms^{-1} and 0.4 ms^{-1}, respectively (Figure 22 (c)). The results for El-Norte showed a similar current direction as the one found in Figure 21 (d), however the current was weaker than the one found from the ADV located at M4.

The ADV positioned at M6 (second sandbar 1.25 m depth) showed similar current direction as seen from the ADV located at M5 (Figure 23 (a)). However, the SB cross-shore current velocity was higher by ~ 0.2 ms^{-1}. During LB the cross-shore current direction varied between onshore and offshore, while the longshore current remained eastward during the whole period (Figure 23 panel b). On the other hand, during SB the cross-shore current was enhanced and increased by 0.2 ms^{-1}, but the longshore current did not show an increase when compared to LB longshore currents (Figure 23 panel c). Finally, the El-Norte longshore current velocity attained a maximum of 0.31 ms^{-1} eastward, while the cross-shore maximum velocity was 0.22 ms^{-1} in the onshore direction (Figure 23 (d)). Table 4 and 5, show the difference between the basic statistics of the cross and lonshore current velocities obtained from M4, M5, and M6.

Table 4. Cross-shore current velocity statistics.

Cross-shore velocity (ms^{-1})						
	LB		SB		El-Norte	
Position	Average	Max	Average	Max	Average	Max
M4	0.038	0.055	0.273	0.512	-0.428	-0.307
M5	0.007	0.023	0.061	0.135	-0.036	0.011
M6	0.011	0.039	0.101	0.253	-0.166	-0.067

Table 5. Longshore current velocity statistics.

Longshore velocity (ms^{-1})						
	LB		SB		El-Norte	
Position	Average	Max	Average	Max	Average	Max
M4	0.001	0.017	-0.139	0.027	-0.078	-0.015
M5	0.011	0.035	0.063	0.146	-0.24	-0.084
M6	0.026	0.041	0.022	0.056	-0.221	-0.042

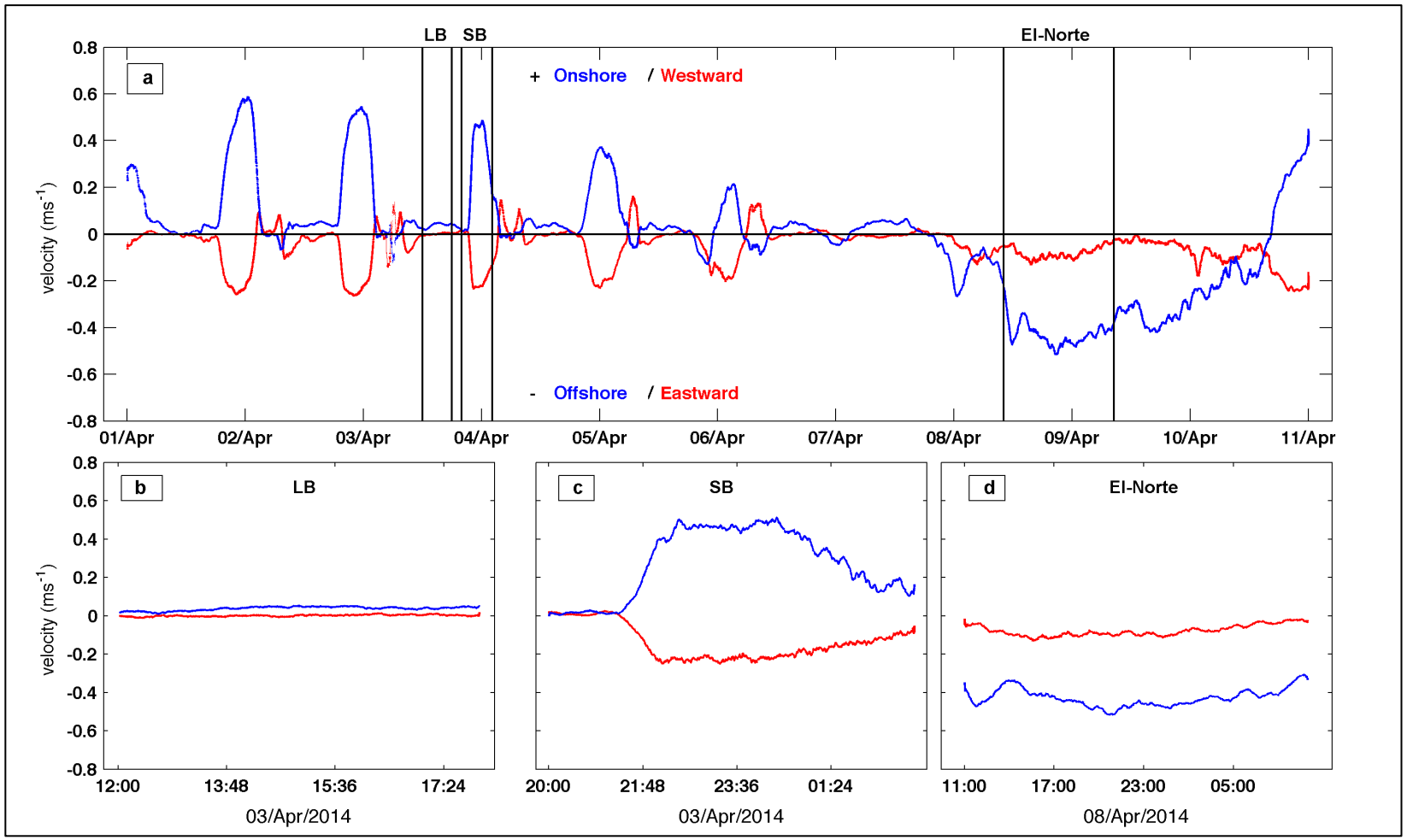

Figure 21. Cross/longshore current at M4 (a) 15 minutes average velocity from April 1st to April 11th (b) 5 minute average current velocity for LB (c) 5 minute average current velocity for SB (d) 5 minute average current velocity for El-Norte.

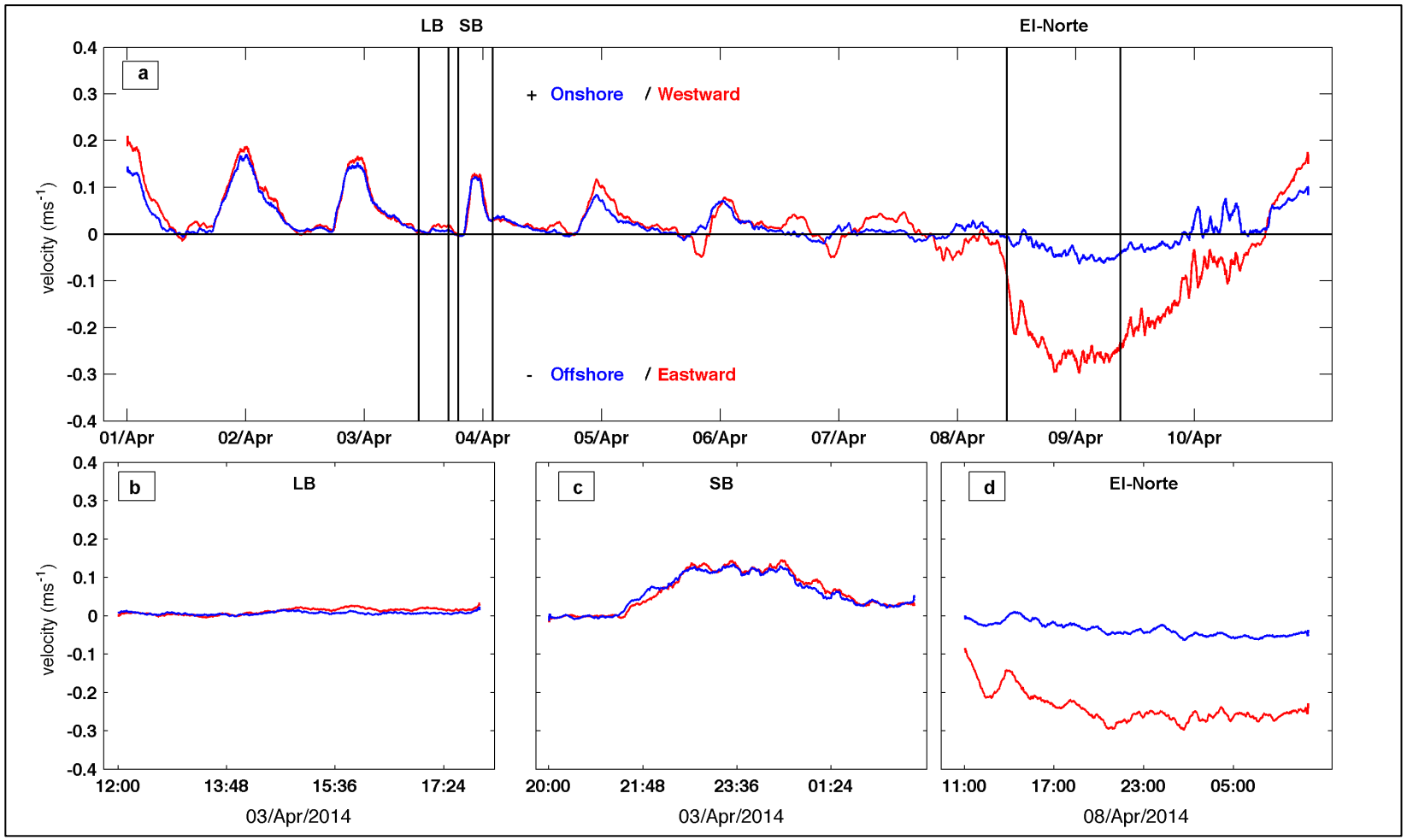

Figure 22. Cross/longshore current at M5 (a) 15 minutes average velocity from April 1st to April 11th (b) 5 minute average current velocity for LB (c) 5 minute average current velocity for SB (d) 5 minute average current velocity for El-Norte.

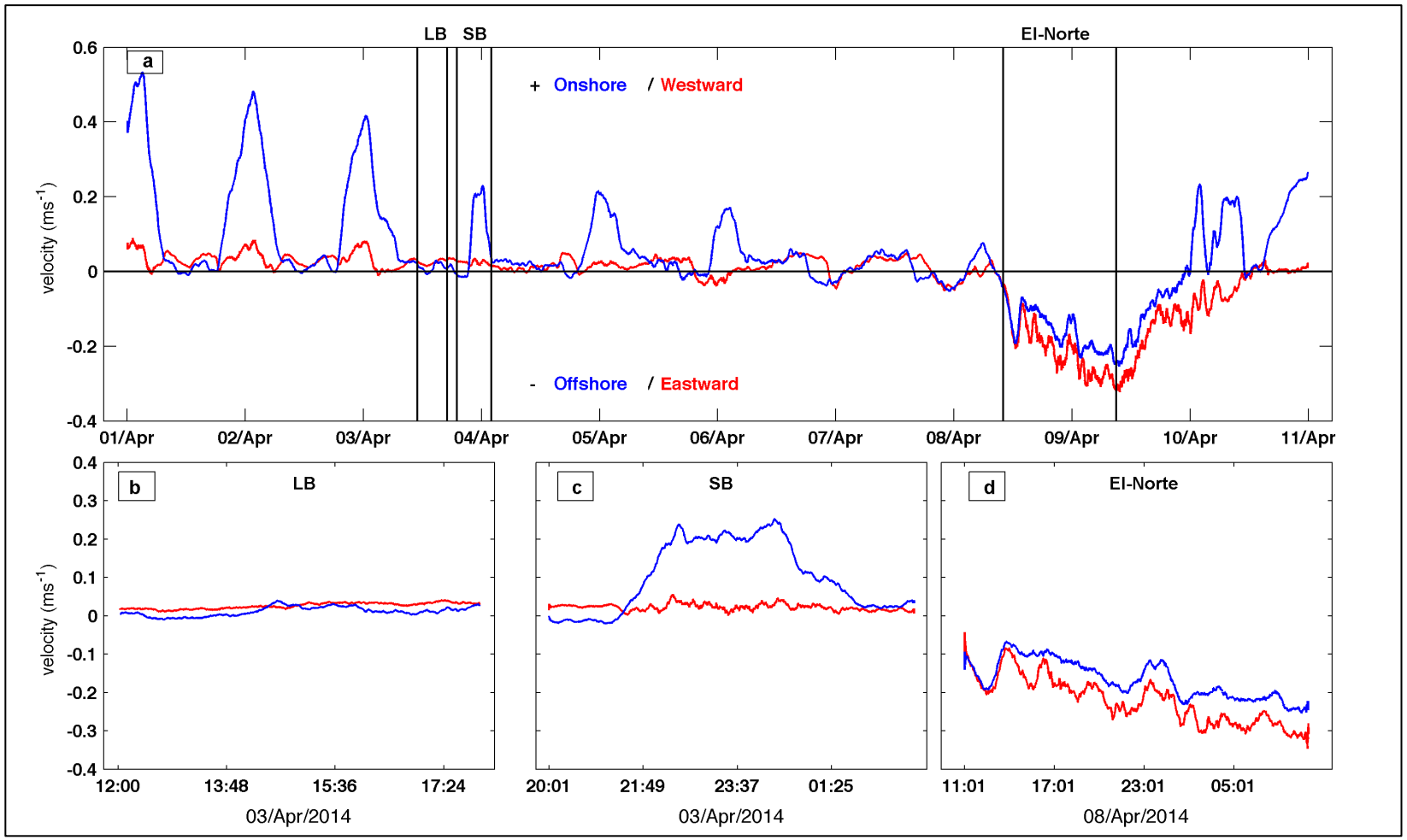

Figure 23. Cross/longshore current at M6 (a) 15 minutes average velocity from April 1st to April 11th (b) 5 minute average current velocity for LB (c) 5 minute average current velocity for SB (d) 5 minute average current velocity for E-Norte.

4. DISCUSSION

The observations suggest that both El-Norte and SB events have a dramatic impact on the nearshore hydrodynamic conditions. Both SB and El-Norte have resulted in wind waves dominated environment. In addition, these events resulted in a significant increase in current velocity due to the increase in wind speed, which led to the increase of τ_w. This section addresses the comparison between the effect of El-Norte, SB, and the normal conditions (LB) in terms of sediment grain size variability and distribution, hydrodynamic changes, and the changes in the beach morphology.

4.1. Hydrodynamics

4.1.1. Wave comparison and assessment

The increase of both H_s and T_s values were found to be highest during El-Norte events compared to SB H_s and T_s. Estimated H_s and T_s at M4 during SB and LB were too low to be considered reliable. This may be a result of a malfunction in the ADV pressure sensor. Therefore, the values of H_s and T_s will not be discussed for the M4 position but an interpolated overall average will be taken into account instead.

One of the main reasons behind the increase of H_s and T_s was the dramatic growth of τ_w. It was observed that the increase in wind speed is correlated with an increase in τ_w mainly during the period when the wind direction was steady (see Figure 9, section 3.1). In other words, the results suggest that the wind speed and $\tau_w$were the main forces driving the increase in the wave characteristics within the study site, where H_s and T_s in all positions were found to be increasing exponentially as the wind blows in

a steady direction. LB resulted in a calmer wave environment than waves observed during both SB and El-Norte, where LB had a minor effect on the H_s and T_s due to the low wind speed veering from the south (mean direction 138^o). In addition, the absence of fetch (i.e. the length of the water surface over which the wind can blow over a period of time) eventually resulted in low values of τ_w. Thus, lower values of H_s and T_s were found during LB.

4.1.2. Current comparison and assessment

Strong cross-shore and longshore currents were observed in the surf zone during events of high H_s (e.g. SB and El-Norte), while weak current velocity was observed during LB due to low wind speed and H_s which resulted in little energy being transferred into the water column. During SB strong onshore current and an eastward longshore current were dominant at M4. A strong onshore current was observed during SB, however, significantly stronger offshore current was observed during El-Norte. The reason for having a strong eastward current might be a result of the wave breaking and the bed topography at M4. However, further analysis is needed to gain a better understanding of the current behavior.

M5 had a cross-shore and longshore current with the same pattern and nearly the same velocity (onshore and westward) during both SB and LB. The same results were found for LB events where low current velocities were observed. Furthermore, SB events had a significant increase in both cross-shore and longshore current velocities. This increase was a result of the increase in the energy introduced to the system via wind stress, which increased H_s values during SB. In addition, the presence of westward

longshore currents might be due to the waves propagating in the direction of the wind. The increase in wave energy during El-Norte may have resulted in the strong undertow current at M5. *Stone et al.* [2004] observed similar current results during cold front passage. M6 had similar results as M5, but the longshore current was significantly lower than at M5 during both periods (LB and SB). On the other hand, an increase in the longshore current velocity was observed during El-Norte as a result of the increase in the H_s. In addition, the strong offshore velocities indicated undertow current existed at M6.

4.1.3. TKE, ε, τ_b

In order to investigate the effect of the hydrodynamic parameters on the surf zone it was important to compute bottom shear stress (τ_b), turbulent kinetic energy (TKE) and turbulent kinetic energy dissipation (ε) using measurements obtained from the ADVs at locations M4, M5, and M6. Figure 24, 25, and 26 shows the estimated TKE (panel a), ε (panel b), and τ_b (panel c) for locations M4, M5, and M6, respectively. According to Figures 24, 25, and 26, LB had a low estimated TKE, ε, τ_b, where these values were enhanced during SB due to wave breaking, and strong long/cross-shore currents. The most noticeable increase was observed during El-Norte due to the increase in τ_w, which resulted in increasing the wave height in the surf zone. Table 6 shows a comparison between estimated average and maximum values of TKE, ε, τ_b during all selected events based on their physical locations.

Measured surf zone TKE values ranged from 10^{-2} m^2s^{-2} to 10^{-1} m^2s^{-2}, ε values varied between 10^{-6} m^2s^{-3} (LB) and 10^{-3} m^2s^{-3} (El-Norte). Similar results were observed by *Feddersen et al.* [2007] and *Trowbridge and Elgar* [2001]. *Trowbridge and Elgar*

[2001] observed the range of ε in the surf zone to be from 10^{-5} m^2s^{-3} (calm waves) to 10^{-4} m^2s^{-3} (SB). The observed τ_b during the field measurements in this study ranged from 0.5 Nm^{-2} at LB to 21 Nm^{-2} during El-Norte. Comparing observed τ_b to other τ_b study results such as the study by *Jing and Ridd* [1996] which showed values between 0.25- 6 Nm^{-2} in a bay. On the other hand, *Dufois et al.* [2008] study observed τ_b values ranging between 1-10 Nm^{-2} within the surf zone, which is still less than found in this study. However, Tomás et al. [2012] had τ_b values ranging between 2-70 Nm^{-2} within the surf zone during strong wind events.

All M4 measurements (located at the first sandbar) displayed the highest TKE and ε, where it is assumed that enhancements in TKE values were due to transfer of momentum from the broken waves. However, position M5 (trough) had the highest estimated τ_b, approximately 4 Nm^{-2} during SB and 21 Nm^{-2} during El-Norte, which was due to the intense longshore velocity that was present at that location.

Moreover, high H_s values were present during both SB and El-Norte and may have resulted in the growth of TKE, ε, and τ_b. The second sandbar, where M6 was located, showed relatively high values of ε, averaging 1.8×10^{-4} m^2s^{-3} during SB and increasing significantly to 1.7×10^{-3} m^2s^{-3} during El-Norte. Estimated values of τ_b at M6 were found to be higher than the estimated values for the first sandbar (M4), which may be a result of the accumulative effect of larger waves propagating and breaking over the sand bar during El-Norte, in addition to increasing the estimated values of both TKE and ε.

The overall analysis of all these observations suggests that high turbulence is occurring over both sandbars and the trough. Even though SB estimated τ_b values were lower than the values found during El-Norte, they still are critical to modification of beach profile. Furthermore, the relatively high values of τ_b found during El-Norte combined with the strong offshore current explains the presence of the undertow currents found at locations M4, M5, and M6.

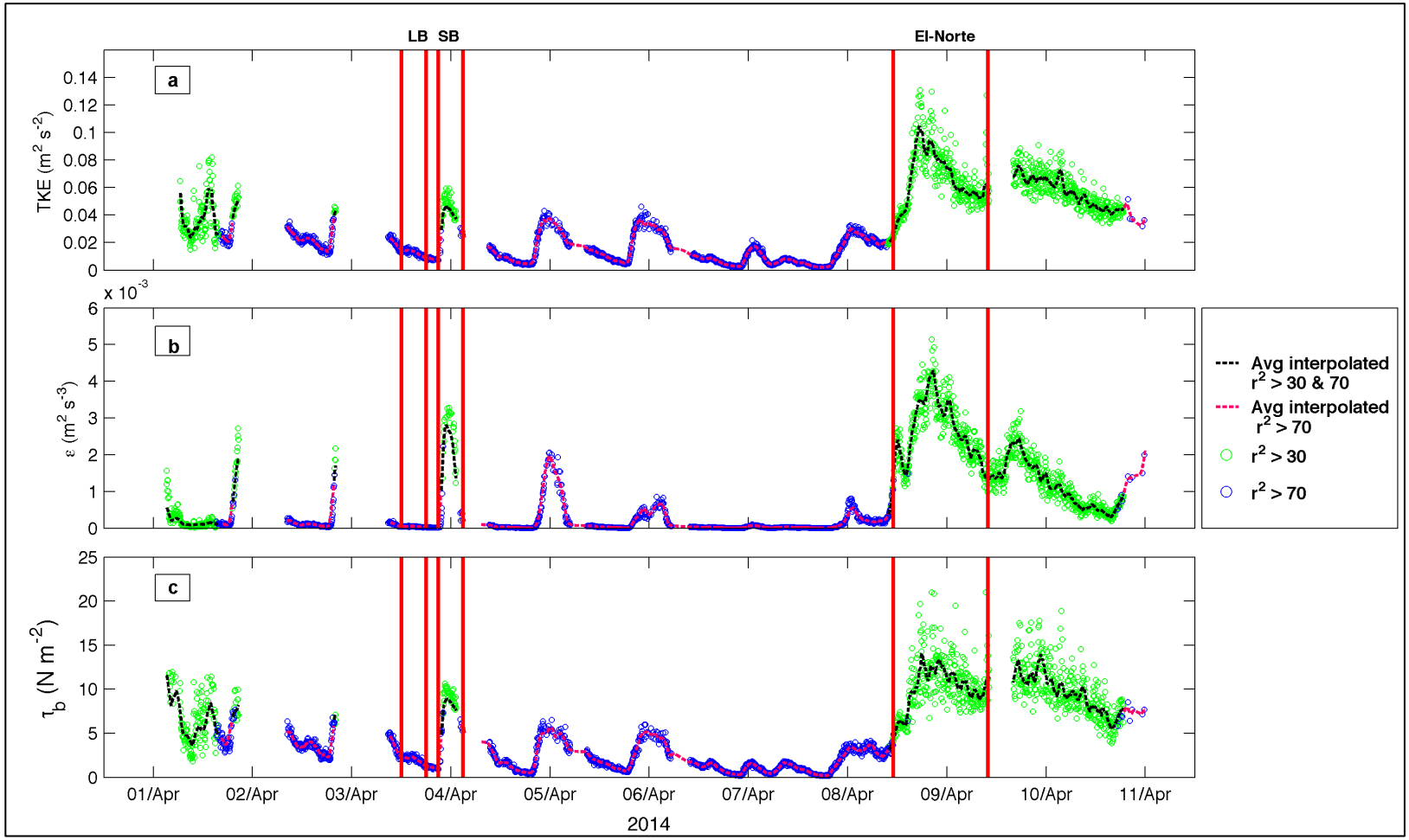

Figure 24. Computed TKE, ε, τ_b from the ADV positioned at M4 (a) 4 minutes average TKE (b) 4 minutes average , ε (c) 4 minutes average τ_b.

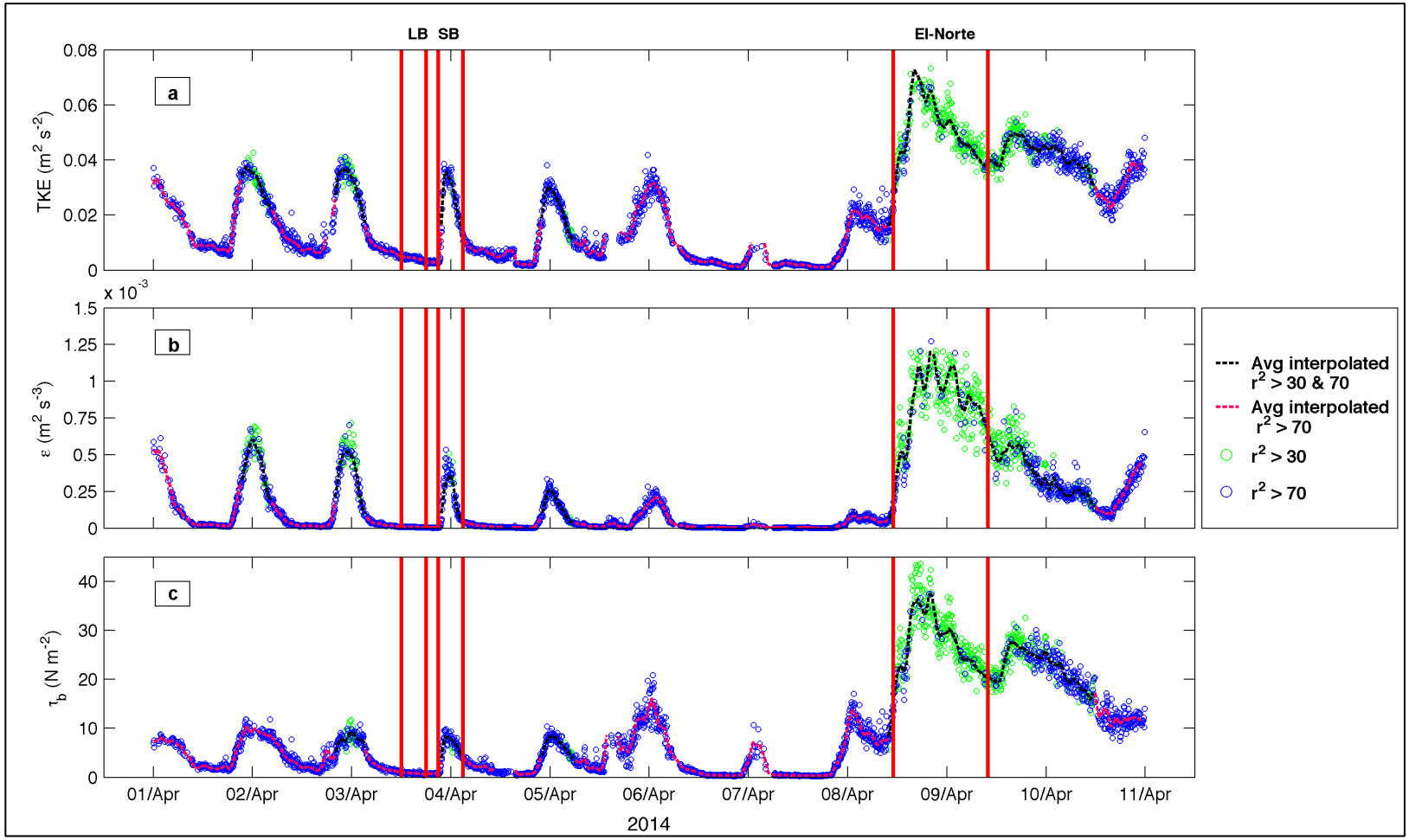

Figure 25. Computed TKE, ε, τ_b from the ADV positioned at M5 (a) 4 minutes average TKE (b) 4 minutes average , ε (c) 4 minutes average τ_b.

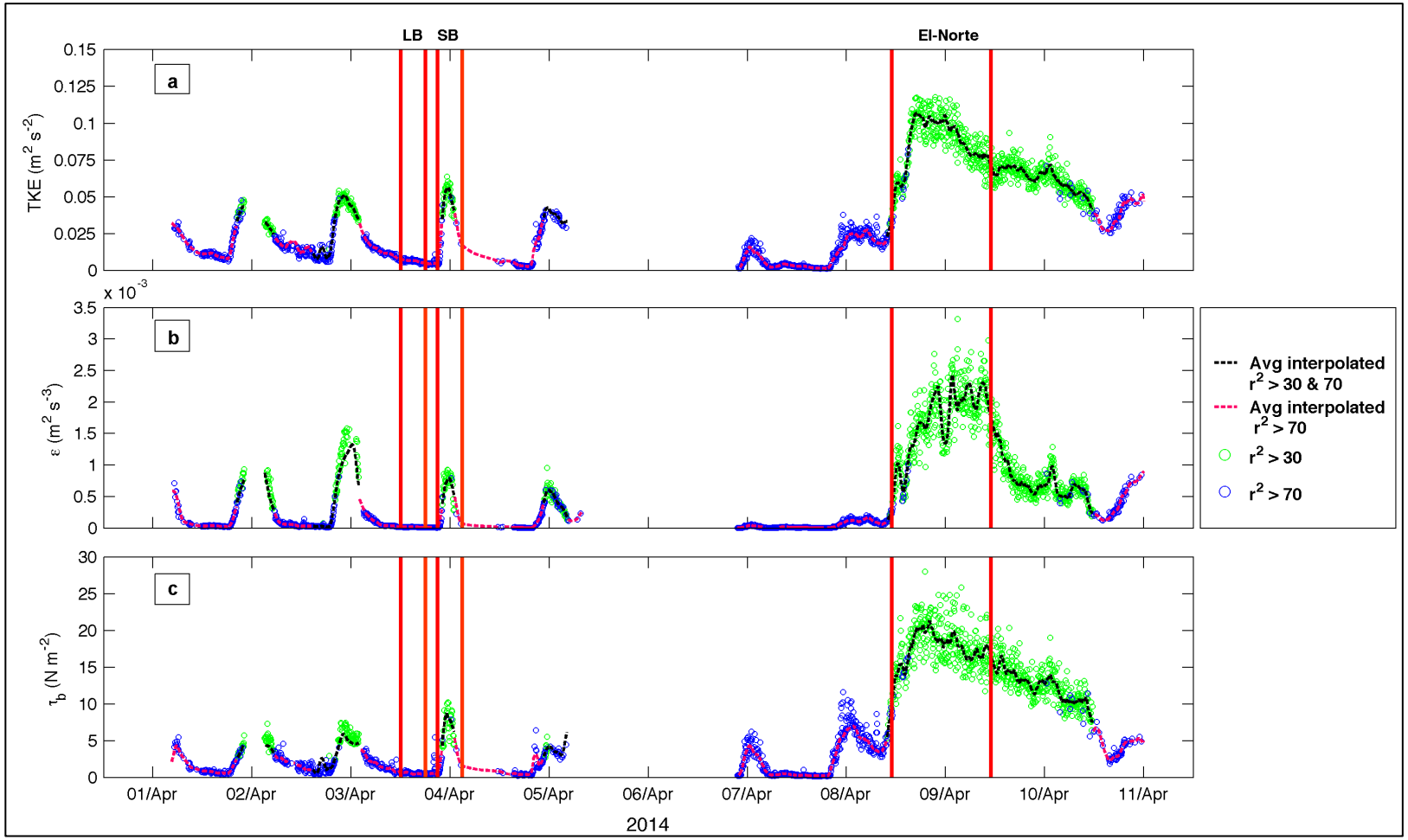

Figure 26. Computed TKE, ε, τ_b from the ADV positioned at M6 (a) 4 minutes average TKE (b) 4 minutes average , ε (c) 4 minutes average τ_b.

Table 6. Mean and maximum computed TKE, ε, τ_b for positions M4, M5, and M6 during SB, LB, and El-Norte.

TKE (m^2s^{-2})						
	Average			Max		
Position	LB	SB	El-Norte	LB	SB	El-Norte
M4	1.12×10^{-2}	2.25×10^{-2}	4.56×10^{-2}	1.52×10^{-2}	4.01×10^{-2}	4.56×10^{-2}
M5	3.79×10^{-3}	1.72×10^{-2}	5.11×10^{-2}	4.88×10^{-3}	3.61×10^{-2}	7.01×10^{-2}
M6	6.31×10^{-3}	1.81×10^{-2}	7.62×10^{-2}	7.41×10^{-3}	5.11×10^{-2}	8.31×10^{-2}
ε (m^2s^{-3})						
M4	3.9×10^{-5}	1.3×10^{-3}	2.7×10^{-3}	6.8×10^{-5}	3.5×10^{-3}	4.3×10^{-3}
M5	7.0×10^{-6}	1.4×10^{-4}	8.7×10^{-4}	1.2×10^{-5}	3.7×10^{-4}	1.3×10^{-3}
M6	1.6×10^{-5}	1.8×10^{-4}	1.7×10^{-3}	2.5×10^{-5}	7.8×10^{-4}	2.4×10^{-3}
τ_b (Nm^{-2})						
M4	1.82	5.82	10.17	2.64	9.53	14.51
M5	0.82	4.33	21.83	1.59	8.31	23.97
M6	0.55	2.31	17.63	0.96	7.73	21.31

4.2. Sediment and beach profile

4.2.1. Cross-shore sediment grain size variability and distribution during SB/LB and El-Norte

The sediment grain size distribution observations (Section 3.2.1) suggest that during SB fine sand was the most dominant fraction in the surf zone (M4, M5, and M6). Locations M2 and M3 had a higher percentage of medium sand. This may be a result of the increase of wave bores, resulting in suspending the finer sediment fraction. Moreover, it can be observed that SB showed a decrease in fine sand content at M1 and M2. This trend was even more prevalent at M3, where the increase in H_s values seemed to have more of an effect on suspension and transport of fine sand, resulting in the relative increase of coarser sediment fractions. By observing the changes in the beach profiles between LB and SB, it can be seen that SB caused more erosions between M3 and M4 and an increase in elevation at M6. This suggests that the increase in fine sand was due to the prevailing onshore currents associated with high values of τ_b, resulting in suspension and subsequent deposition of fine sand. In addition, an increase in medium sand has been noticed at M2, M4, and M6, yet the highest increase of 12% was observed at M3. These observations indicate that this increase was mainly due to high H_s and τ_b values associated with the onshore currents present at M4, M5, and M6. Fine sediment was suspended leaving the coarse grains behind.

During El-Norte grain size varied from fine to medium sand. Correlating the temporal and spatial fine sand variation with H_s suggests that the increasing H_s values at the beginning of El-Norte (11:00-16:00) due to the rapid increase in wind velocity were

associated with a decrease of fine sand at M1 and M2 and an increase of fine sand at M3. The beach profile changes show erosion over the first and second sandbar and accretion moving shoreward. Hence, positions M4, M5, and M6 had a much higher percentage of fine sand than any of the other positions. This may be due to deposition of sand over these locations or due to low turbulence levels incapable of suspending fine sand. As time passed, a noticeable overall sediment increase was found in locations M1 and M2, while a decrease was observed at M3, which may be a result of sand being transported during wave boring and/or backwash processes, which may be one of the main reasons that led to the increase of fine sand at M1. It can be observed that at locations M1 to M3 El-Norte had more medium coarser sand and fine gravel fractions than LB and SB. This can be explained by the cumulative effect of waves breaking and the energy introduced to the study area during El-Norte that had more effect on the sediment cross-shore transport or more energy to suspend fine sand than SB/LB.

In order to understand the effect of different wind climates on the sediment, grain size variability statistics needed to be included; therefore d_{50} (Figure 27) and other grain size distribution statistics (Figures 28 (LB and SB) and 29 (El-Norte Period)) were computed (explained in section 2.2.1). The distribution skewness can be obtained from appendix D. The d_{50} results varied between 0.2 mm and 1.8 mm in and near the swash zone. During SB d_{50} values were higher than the ones during El-Norte at M1 and M2, while M3 observed higher d_{50} values during El-Norte. The increase in d_{50} values at M2 during SB could be a result of more accretion at that location or due to the turbulence

induced by wave breaking which may predominantly entrain finer sediment into the water column.

According to Figures 28 and 29 during LB and SB there was no significant change in the grain size distributions. Sediments in the swash zone (M1 and M2) and in the inner surf zone (M3) were found to be coarser than the ones found further offshore, which may be a result of having the fine sediment suspended during high wave energy periods, ultimately increasing the relative fraction of coarser sediment.

In terms of sorting, position M1 was characterized as well-sorted during both LB and SB, while M2 and M3 were observed to be moderately well-sorted. However, the increase in the bed turbulence produced by surface forcing and wave bores resulted in a poorly-sorted distribution at M4 and M5. During LB, M6 had a very well-sorted distribution, while at SB the increase in the turbulence and other hydrodynamic parameters may have resulted in a well-sorted distribution. As specified previously (section 2.2), sediment samples during El-Norte were limited to M1, M2 and M3. The sediment grain size distribution during El-Norte ranged between poorly to moderately well-sorted at positions M1 and M2, while M3 was well-sorted at the beginning of the event, and shifted to poorly-sorted at 04:00, at which point H_s and wind speed had reached maximum values.

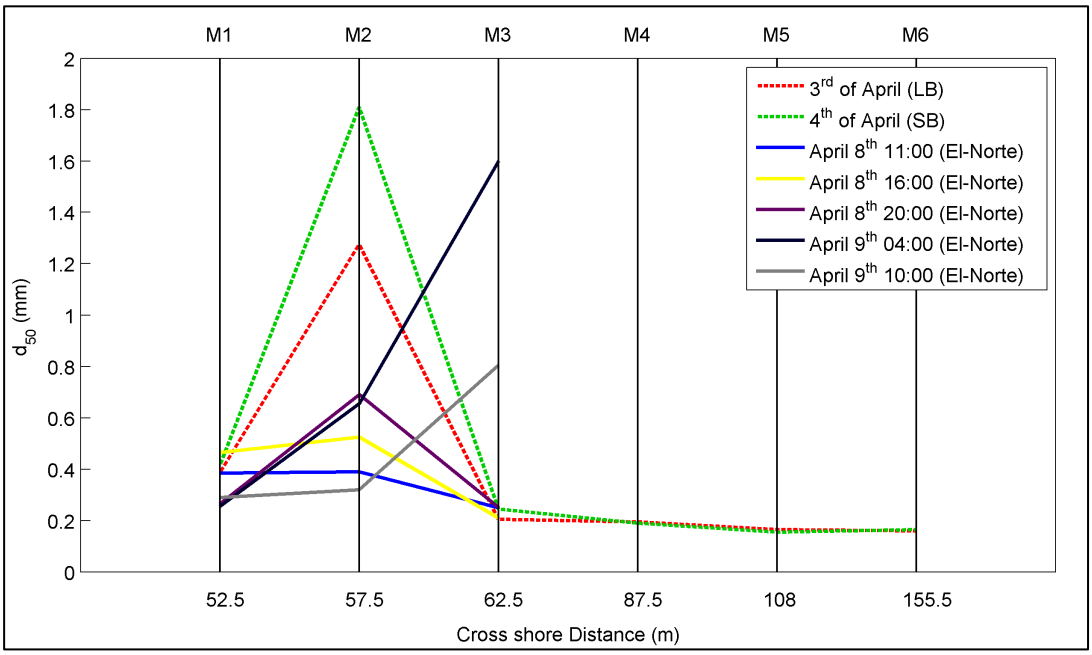

Figure 27. Estimated d_{50} for LB, SB (positions M1-M6), and El-Norte (positions M1-M3).

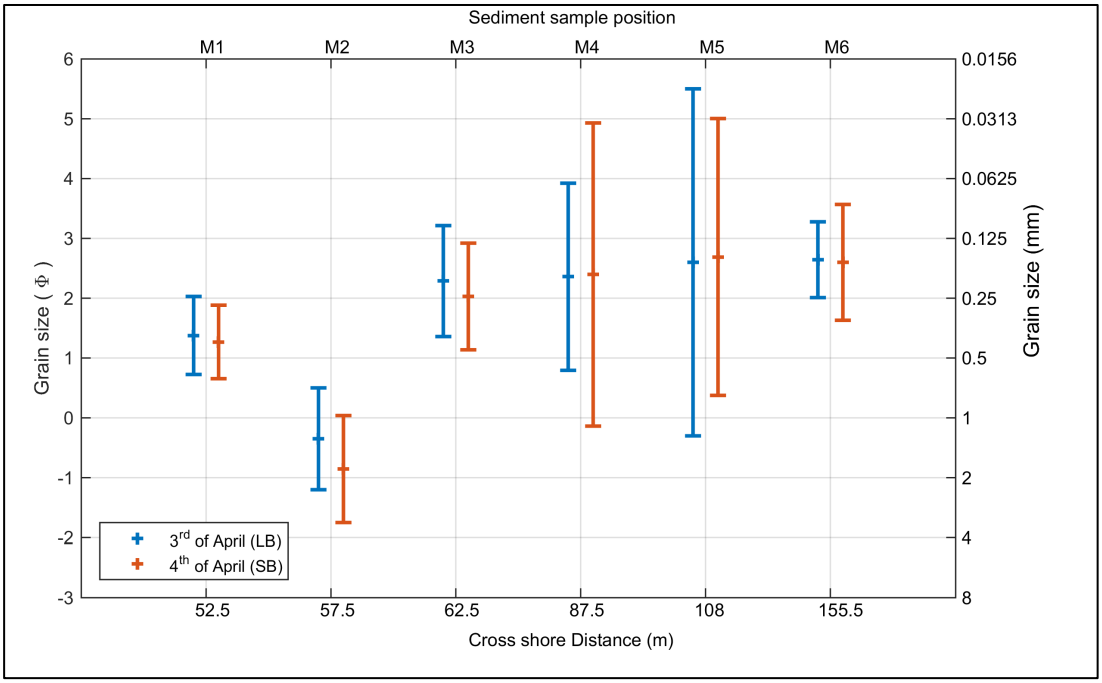

Figure 28. Grain size distribution during LB (April 3rd) and SB (April 4th).

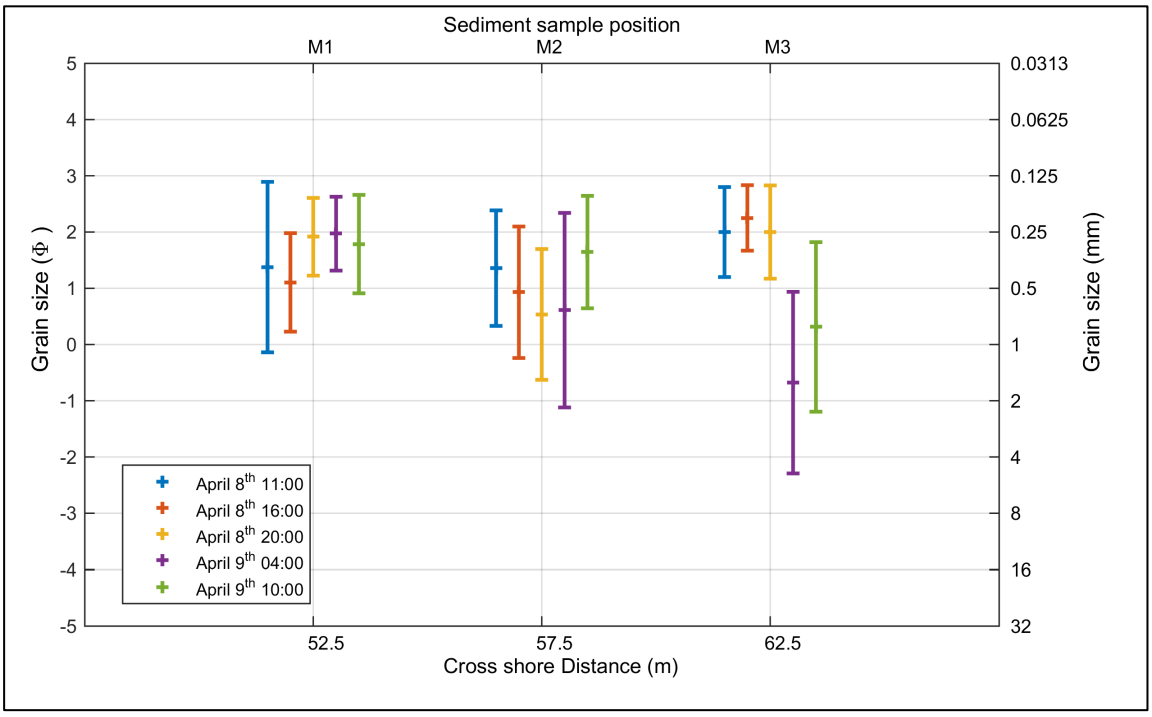

Figure 29. Grain size distribution during El-Norte.

4.2.2. Beach profile and sandbar migration

Beach profile analysis suggests that during the LB to SB transition the profile encountered relatively high elevation changes. The erosion that occurred at M1, M2, and M3 may be due to wave boring/breaking and as a result the increase in τ_b. Furthermore, a migration of the sandbars was observed during SB that might be a result of the strong onshore current along with the increase in τ_b that was present at these locations. However, different results were observed during El-Norte, where the profile became 1.5° steeper (46-58 m) due to the accretion between 40 m and 60 m. The area between 60 m to 180m was dominated by erosion due to the increase in H_s and τ_b. The increase in τ_b and the offshore current that was present during El-Norte explain the slight migration of

the sands bars. *Hoefel and Elgar* [2003], *Hsu et al.* [2006], and *Fernández-Mora et al.* [2015] suggested that large waves breaking over sandbars can cause a strong offshore current (undertow) resulting in the migration of these sandbars offshore. During SB waves tend to be smaller and might break further onshore, resulting in sandbars migrating onshore. Figure 30, represents a schematic displaying the conceptual observed feedback mechanisms relating hydrodynamics and beach profile changes during El-Norte and SB.

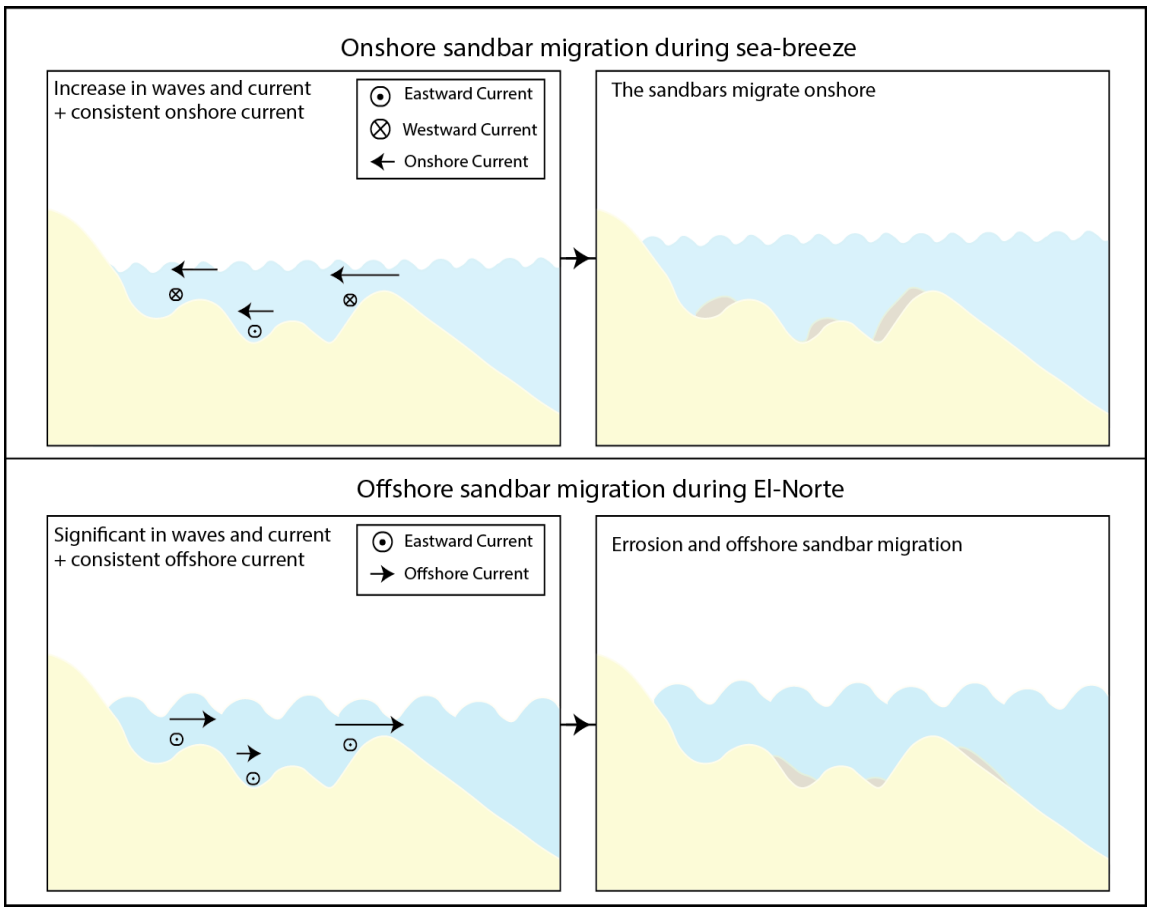

Figure 30. Concept model of sandbar migration during SB and El-Norte.

4.3. Estimated erosion/deposition and overall comparison

A full comparison in terms of average grain sizes and H_s of all three events can be seen in Figure 31. It can be observed that grain size varied between 0.1 to 0.4 mm, except at M2, which had a constant value of 0.275 mm during both LB and SB. El-Norte showed a significant increase in H_s in addition to the coarser grain size that was found between M2 and M3.5. Erosion and accretion (see Figure 32) for positions M1 to M3 were estimated using height adjustments of the instruments.

Observations from Figure 32, suggest that sediment deposition was dominant during LB, especially at M3 during the onset of the LB event. Locations M1 to M3 during the beginning of SB event were found to be dominated by erosion, which may be a result of wave boring and enhancement of the undertow current. However, accretion between 1 cm to 2 cm occurred at the end of the SB, which may be a result of the decrease in H_s values resulting in settling of the suspended sediment. Figure 32 (b) shows that during post El-Norte accretion occurs, where wind velocity, H_s, and current velocity were low, resulting in a calm environment and therefore less sediment movement. However, during post El-Norte 2 to 4 cm erosion occurred at M1, M2, and M3.

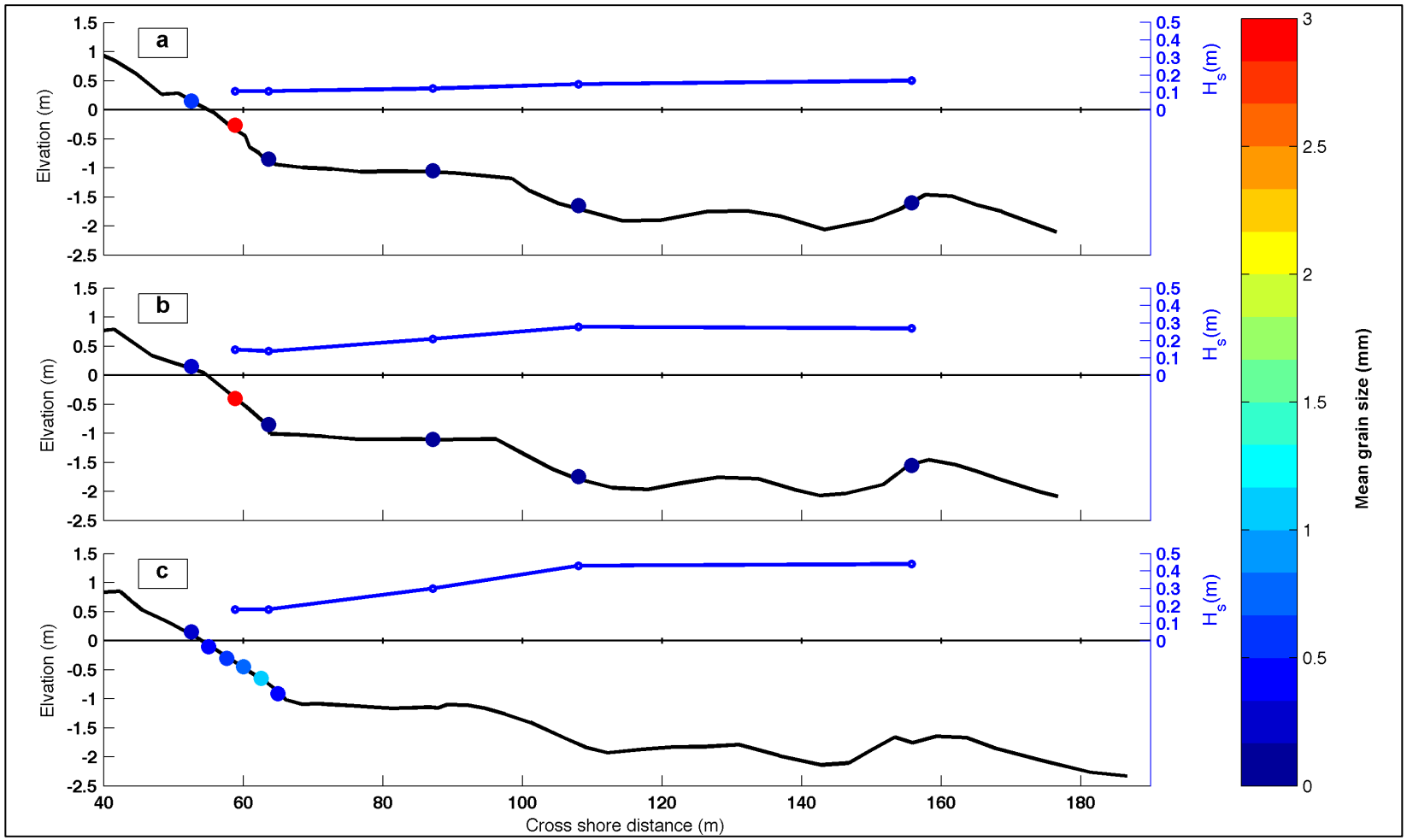

Figure 31. Beach profile variation, mean grain size, and mean H_s (a) LB (b) SB (c) El-Norte.

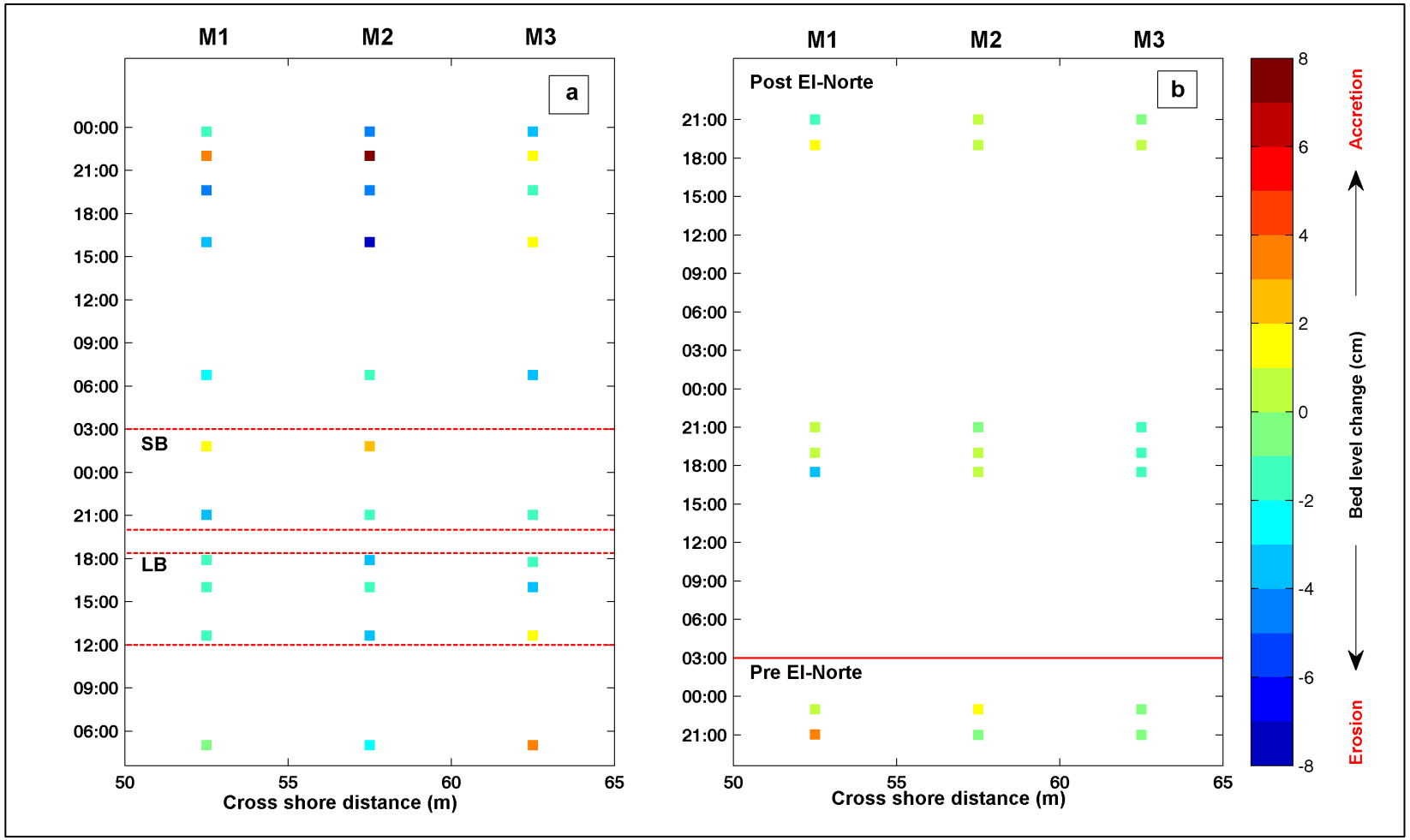

Figure 32. Swash zone estimated erosion/accretion measurements for (a) LB and SB (b) pre and post El-Norte.

5. CONCLUSIONS

The primary purpose of this study is to compare and assess the effects of mesoscale pressure systems, i.e., cold front and local pressure systems (land and sea breezes) on the surf zone hydrodynamics and morphodynamics, with a particular focus on the effect of both sediment size variation and beach profile. To this end, analyses of hydrodynamics, sediment size distributions, and beach profile changes in the surf and swash zones were conducted for three different forcing conditions. The study results suggest that the area is characterized by a diurnal SB/LB, where the hydrodynamics and morphodynamics in the surf zone are dominated by the shift between SB and LB. In addition the most significant abrupt changes to the morphodynamics were caused by El-Norte.

Hydrodynamic parameters were higher during El-Norte compared to the ones recorded during SB and LB. The field observations of TKE, ε, τ_b were also higher during periods of increased wind stress. El-Norte τ_b values were found to be significantly higher than estimated τ_b values during SB. In addition, H_s values were found to be 0.24 m higher further offshore in the surf zone during El-Norte than during SB. The increase of H_s at M4, M5, M6 resulted in a strong offshore current (undertow) during El-Norte, while onshore current was more dominated during both LB and SB events.

The sediment analyses have illustrated a significant relationship between changes in SB and LB waves with the grain size distribution. The resulting increase in H_s, TKE,

ε, τ_b, and current velocity during the period of SB resulted in a poorly-sorted sand distribution in the surf zone (M4-M6) and a moderately well-sorted distribution in the swash zone (M1-M3). However, El-Norte resulted in increasing the turbulence within the system resulting in M1 and M2 being dominated by fine sand fractions with a moderately sorted distribution, while M3 was dominated by medium sand with moderate sorting at the beginning of the event and poor sorting at the end. Overall, the effect of increasing the hydrodynamic parameters during SB has not resulted in a significant change in the beach profile compared to LB, however, it was noticed that it resulted in the erosion of the beach step at 58 m. In addition, onshore currents during SB resulted in a slight migration of both sandbars shoreward, which are generated from increasing the wave energy leading to the increase in τ_b. However, strong undertow currents, which are caused due to the increase in the wave height and period, observed during El-Norte led to erosion of the swash and surf zone, in addition to the offshore sandbar migration. Furthermore, sandbar migration was found to be more controlled by cross-shore current, when mainly due to the strength of undertow currents the sandbar migration will tend to be offshore, such findings have been reported by *Hoefel and Elgar* [2003], and *Hsu et al.* [2006].

It can be stated that El-Norte skewed sediment towards more coarse grains while LB/SB had more fine sand percentages. As El-Norte had significantly increased ε, and τ_b, resulting in suspending greater fraction of fine grains than SB and LB. Finally, it is safe to conclude that LB created a more depositional environment in the surfe zone and the swash zone, while SB caused more erosion in the swash zone and deposition of

sediment in the surf zone, especially between 90 m and 100 m, and 152-160 m. In contrast, El-Norte was found to be more effective in the erosion of the swash zone, and the surf zone sandbars. However, deposition of sand was found in the inner surf zone (between 63-68 m) during El-Norte.

In summary, the first study hypothesis was observed to be true as swash zone sediment distributions during El-Norte were found to be skewed towards coarser grains compared to sea-breeze event. Onshore sandbar migration and deposition of sediment within the surf zone were observed during SB, which agrees with the second hypothesis. The third hypothesis was supported by the observation of significant erosion of the beach profile that occurred during El-Norte. Finally the last hypothesis was observed to be true, as during El-Norte strong offshore currents existed over M4, M5, and M6 affecting the morohodynamics (i.e., offshore sandbar migration).

REFERENCES

Abuodha, J. O. Z. (2003), Grain size distribution and composition of modern dune and beach sediments, Malindi Bay coast, Kenya, *Journal of African Earth Sciences*, *36*(1-2), 41-54, doi:10.1016/s0899-5362(03)00016-2.

Appendini, C. M., P. Salles, E. T. Mendoza, J. López, and A. Torres-Freyermuth (2012), Longshore sediment transport on the northern coast of the Yucatan Peninsula, *Journal of Coastal Research*, *285*, 1404-1417, doi:10.2112/jcoastres-d-11-00162.1.

Babaeyan-Koopaei, K., D. A. Ervine, P. A. Carling, and Z. Cao (2002), Velocity and turbulence measurements for two overbank flow events in river severn, *Journal of Hydraulic Engineering*, *128*(10), 891-900, doi:10.1061/(asce)0733-9429(2002)128:10(891).

Babanin, A. (2011), *Breaking and dissipation of ocean surface waves*, Cambridge University Press, United State of America, New York, doi:10.1017/cbo9780511736162.

Biron, P. M., S. N. Lane, A. G. Roy, K. F. Bradbrook, and K. S. Richards (1998), Sensitivity of bed shear stress estimated from vertical velocity profiles: the problem of sampling resolution, *Earth Surface Processes and Landforms*, *23*(2), 133-139, doi:10.1002/(sici)1096-9837(199802)23:2<133::aid-esp824>3.0.co;2-n.

Biron, P. M., C. Robson, M. F. Lapointe, and S. J. Gaskin (2004), Comparing different methods of bed shear stress estimates in simple and complex flow fields, *Earth Surface Processes and Landforms*, *29*(11), 1403-1415, doi:10.1002/esp.1111.

Brammer, H. (2014), Bangladesh's dynamic coastal regions and sea-level rise, *Climate Risk Management*, *1*, 51-62, doi:10.1016/j.crm.2013.10.001.

Brinkkemper, J. A., T. Freyermuth, E. Mendoza, P. Salles, and B. Ruessink (2013), Parameterization of wave run-up on beaches in Yucatan, Mexico: a numerical study, *Coastal Dynamics*, *25*(225-233).

Çelikoğlu, Y., Y. Yüksel, and M. S. Kabdaşli (2006), Cross-shore sorting on a beach under wave action, *Journal of Coastal Research*, *223*, 487-501, doi:10.2112/05-0567.1.

Conner, W., J. Day, R. Baumann, and J. Randall (1989), Influence of hurricanes on coastal ecosystems along the northern Gulf of Mexico, *Wetlands Ecology and Management*, *1*(1), 45-56, doi:10.1007/bf00177889

Curtarelli, M., E. Alcântara, C. Rennó, and J. Stech (2013), Effects of cold fronts on MODIS-derived sensible and latent heat fluxes in Itumbiara reservoir (Central Brazil), *Advances in Space Research*, *52*(9), 1668-1677, doi:10.1016/j.asr.2013.07.037.

Dean, R. (1991), Equilibrium beach profiles: Characteristics and applications, *Journal of Coastal Research*, *7*(1), 53-84.

Dean, R., and R. Dalrymple (2002), *Coastal processes with engineering applications*, Cambridge University Press, Cambridge, United Kingdom, doi:http://dx.doi.org/10.1017/CBO9780511754500.

Dufois, F., P. Garreau, P. Le Hir, and P. Forget (2008), Wave- and current-induced bottom shear stress distribution in the Gulf of Lions, *Continental Shelf Research*, *28*(15), 1920-1934, doi:10.1016/j.csr.2008.03.028.

Dickey, T. D., G. C. Chang, Y. C. Agrawal, A. J. Williams, and P. S. Hill (1998), Sediment resuspension in the wakes of hurricanes Edouard and Hortense, *Geophysical Research Letters*, *25*(18), 3533-3536, doi:10.1029/98gl02635.

Dingler, J. R., and T. E. Reiss (1990), Cold-front driven storm erosion and overwash in the central part of the Isles Dernieres, a Louisiana barrier-island arc, *Marine Geology*, *91*(3), 195-206, doi:10.1016/0025-3227(90)90036-j.

Dolan, R., B. Hayden, and J. Heywood (1978), Analysis of coastal erosion and storm surge hazards, *Coastal Engineering*, *2*, 41-53, doi:10.1016/0378-3839(78)90004-2.

Dragani, W. C. (1999), A feature model of surface pressure and wind fields associated with the passage of atmospheric cold fronts, *Computers & Geosciences*, *25*(10), 1149-1157, doi:10.1016/s0098-3004(99)00074-6.

Enriquez, C., I. J. Mariño-Tapia, and J. A. Herrera-Silveira (2010), Dispersion in the Yucatan coastal zone: implications for red tide events, *Continental Shelf Research*, *30*(2), 127-137, doi:10.1016/j.csr.2009.10.005.

Esteves, L., J. E. Toldo, S. Dillenburg, and L. Tomazelli (2002), Long- and short-term coastal erosion in southern brazil, *J ournal of Coastal Research*, *36*, 273-282.

Feddersen, F., J. H. Trowbridge, and A. J. Williams (2007), Vertical structure of dissipation in the nearshore, *Journal of Physical Oceanography*, *37*(7), 1764-1777, doi:10.1175/jpo3098.1.

Feddersen, F. (2012), Observations of the surf-zone turbulent dissipation rate, *Journal of Physical Oceanography*, *42*(3), 386-399, doi:10.1175/jpo-d-11-082.1.

Feng, C., C. Hui-Mei, S. Xian-Ze, and X. Dong-Xing (2007), Analysis on morphodynamics of sandy beaches in south China, *Journal of Coastal Research*, *231*, 236-246, doi:10.2112/04-0197.1.

Fernández-Mora, A., D. Calvete, A. Falqués, and H. E. de Swart (2015), Onshore sandbar migration in the surf zone: new insights into the wave-induced sediment transport mechanisms, *Geophysical Research Letters*, doi:10.1002/2014gl063004.

Figueroa-Espinoza, B., P. Salles, and J. Zavala-Hidalgo (2014), On the wind power potential in the northwest of the Yucatan Peninsula in Mexico, *Atmósfera*, *27*(1), 77-89, doi:10.1016/s0187-6236(14)71102-6.

Gallagher, E. L., S. Elgar, and R. T. Guza (1998), Observations of sand bar evolution on a natural beach, *Journal of Geophysical Research*, *103*(C2), 3203-3215, doi:10.1029/97jc02765.

Gallucci, F., and S. Netto (2005), Effects of the passage of cold fronts over a coastal site: an ecosystem approach, *Marine ecology-progress series*(281), 79-92, doi:10013/epic.25294.

Garreaud, R. (2000), Cold air incursions over subtropical South America: mean structure and dynamics, *Monthly Weather Review*, *128*(7), 2544-2559, doi:10.1175/1520-0493(2000)128<2544:caioss>2.0.co;2.

Hinkel, J., R. J. Nicholls, R. S. J. Tol, Z. B. Wang, J. M. Hamilton, G. Boot, A. T. Vafeidis, L. McFadden, A. Ganopolski, and R. J. T. Klein (2013), A global analysis of erosion of sandy beaches and sea-level rise: An application of DIVA, *Global and Planetary Change*, *111*, 150-158, doi:10.1016/j.gloplacha.2013.09.002.

Hoefel, F., and S. Elgar (2003), Wave-induced sediment transport and sandbar migration, *Science*, *299*(5614), 1885-1887, doi:10.1126/science.1081448.

Houser, C., and B. Greenwood (2007), Onshore migration of a swash Bar during a storm, *Journal of Coastal Research*, *231*, 1-14, doi:10.2112/03-0135.1.

Hsu, S. (1988), *Coastal meteorology*, 1 ed., Academic Press, New York.

Hsu, T., S. Elgar, and R. T. Guza (2006), Wave-induced sediment transport and onshore sandbar migration, *Coastal Engineering*, *53*(10), 817-824, doi:10.1016/j.coastaleng.2006.04.003.

Inman, D. (1952), Measures for describing the size distribution of sediments, *Journal of Sedimentary Petrology*, *22*(3), 125-145, doi:10.1306/d42694db-2b26-11d7-8648000102c1865d.

Inman, D. L., and J. Filloux (1960), Beach cycles related to tide and local wind wave regime, *The Journal of Geology*, *68*(2), 225-231, doi:10.1086/626655.

Jing, L., and P. V. Ridd (1996), Wave-current bottom shear stresses and sediment resuspension in Cleveland Bay, Australia, *Coastal Engineering*, *29*(1-2), 169-186, doi:10.1016/s0378-3839(96)00023-3.

Jiménez, C., and E. Ávila (2009), Morphodynamics of carbonate beaches in the Yucatán Peninsula, *Ciencias Marinas*, *35*, 307-320.

Karunarathna, H., J. M. Horrillo-Caraballo, R. Ranasinghe, A. D. Short, and D. E. Reeve (2012a), An analysis of the cross-shore beach morphodynamics of a sandy and a composite gravel beach, *Marine Geology*, *299-302*, 33-42, doi:10.1016/j.margeo.2011.12.011.

Karunarathna, H., J. M. Horrillo-Caraballo, and D. E. Reeve (2012b), Prediction of cross-shore beach profile evolution using a diffusion type model, *Continental Shelf Research*, *48*, 157-166, doi:10.1016/j.csr.2012.08.004.

Karunarathna, H., D. Pender, R. Ranasinghe, A. D. Short, and D. E. Reeve (2014), The effects of storm clustering on beach profile variability, *Marine Geology*, *348*, 103-112, doi:10.1016/j.margeo.2013.12.007.

Kim, S. C., C. T. Friedrichs, J. P. Y. Maa, and L. D. Wright (2000), Estimating bottom stress in tidal boundary layer from acoustic Doppler velocimeter data, *Journal of Hydraulic Engineering*, *126*(6), 399-406, doi:10.1061/(asce)0733-9429(2000)126:6(399).

Kineke, G. C., E. E. Higgins, K. Hart, and D. Velasco (2006), Fine-sediment transport associated with cold-front passages on the shallow shelf, Gulf of Mexico, *Continental Shelf Research*, *26*(17-18), 2073-2091, doi:doi:10.1016/j.csr.2006.07.023.

Kinsman, B. (1965), *Wind waves: their generation and propagation on the ocean surface*, Prentice-Hall, Englewood Cliffs, N.J.

Kobashi, D., F. Jose, and G. Stone (2007), Impacts of fluvial fine fediments and winter storms on a transgressive shoal, off south-central Louisiana, in *Proceedings of the 9th International Coastal Symposium, 858 – 862*, edited, Journal of Coastal Research, Gold Coast, Australia.

Lanckriet, T., J. A. Puleo, G. Masselink, I. Turner, D. Conley, C. Blenkinsopp, and P. Russell (2012), Field measurements of sheet flow sediment transport in the Swash zone, *Coastal Engineering Proceedings*, *1*(33), doi:10.9753/icce.v33.sediment.78.

Lanckriet, T., J. A. Puleo, and N. Waite (2013), A conductivity concentration profiler for sheet flow sediment transport, *IEEE Journal of Oceanic Engineering*, *38*(1), 55-70, doi:10.1109/joe.2012.2222791.

Masselink, G., and C. Pattiaratchi (1998), The effect of sea breeze on beach morphology, surf zone hydrodynamics and sediment resuspension, *Marine Geology*, *146*(1-4), 115-135, doi:10.1016/s0025-3227(97)00121-7.

Mendoza, E., M. Trejo-Rangel, P. Salles, C. Appendini, and J. Lopez-Gonzalez (2013), Storm characterization and coastal hazards in the Yucatan Peninsula, *Journal of Coastal Research*, 65, 790-795.

Miller, A., and J. Thompson (1970), *Elements of meteorology*, Chareles E. Merrill Publushing Co, Columbus,Ohio.

Miner, M. D., M. A. Kulp, D. M. FitzGerald, and I. Y. Georgiou (2009), Hurricane-associated ebb-tidal delta sediment dynamics, *Geology*, *37*(9), 851-854, doi:10.1130/g25466a.1.

Moeller, C., O. Huh, H. Roberts, L. Gumley, and W. Menzel (1993), Response of Lousiana coastal enviroments to a cold front passage, *Journal of Coastal Research*, *9*(2), 434-447.

Otto, G. (1939), A Modified logarithmic probability graph for the interpretation of mechanical analyses of sediments, *SEPM Journal of Sedimentary Research*, *9*(2), 62-76, doi:10.1306/d4269044-2b26-11d7-8648000102c1865d.

Pattiaratchi, C., B. Hegge, J. Gould, and I. Eliot (1997), Impact of sea-breeze activity on nearshore and foreshore processes in southwestern Australia, *Continental Shelf Research*, *17*(13), 1539-1560, doi:10.1016/s0278-4343(97)00016-2.

Pierson, W. J. (1954), An Interpretation of the observable properties of 'sea' waves in terms of the energy spectrum of the Gaussian Record, *Transactions, American Geophysical Union*, *35*(5), 747, doi:10.1029/TR035i005p00747.

Pope, N. D., J. Widdows, and M. D. Brinsley (2006), Estimation of bed shear stress using the turbulent kinetic energy approach—A comparison of annular flume and field data, *Continental Shelf Research*, *26*(8), 959-970, doi:10.1016/j.csr.2006.02.010.

Rajganapathi, V. C., N. Jitheshkumar, M. Sundararajan, K. H. Bhat, and S. Velusamy (2012), Grain size analysis and characterization of sedimentary environment along Thiruchendur coast, Tamilnadu, India, *Arabian Journal of Geosciences*, *6*(12), 4717-4728, doi:10.1007/s12517-012-0709-0.

Rippeth, T. P., J. H. Simpson, E. Williams, and M. E. Inall (2003), Measurement of the rates of production and dissipation of turbulent kinetic energy in an energetic tidal flow: red Wharf Bay revisited, *Journal of Physical Oceanography*, *33*(9), 1889-1901, doi:10.1175/1520-0485(2003)033<1889:motrop>2.0.co;2.

Roberts, H. H., O. K. Huh, S. A. Hsu, and L. J. Rouse (1987), Impact of cold-front passages on geomorphic evolution and sediment dynamics of the complex Louisiana coast, *ASCE*, 1950-1963.

Rutecki, D., T. Dellapenna, E. Nestler, F. Scharf, J. Rooker, C. Glass, and A. Pembroke (2014), Understanding the habitat value and function of shoals and shoal complexes to fish and fisheries on the Atlantic and Gulf of Mexico outer continental shelf. Literature synthesis and gap analysis. Prepared for the U.S. Dept. of the Interior, Bureau of Ocean Energy Management. Contract # M12PS00009. BOEM 2015-012. 176 pp.

Salles, P., A. Souza, A. Torres-Freyermuth, J. López, C. Appendini, E. Menoza, and R. Meza-Padilla (2013), Hydrodynamics over sand dunes in the northern Yucatan peninsula coast, *Coastal Dynamics 2013*, 1407-1416, France.

Senechal, N., G. Coco, B. Castelle, and V. Marieu (2015), Storm impact on the seasonal shoreline dynamics of a meso- to macrotidal open sandy beach (Biscarrosse, France), *Geomorphology*, *228*, 448-461, doi:10.1016/j.geomorph.2014.09.025.

Smith, S. D. (1988), Coefficients for sea surface wind stress, heat flux, and wind profiles as a function of wind speed and temperature, *Journal of Geophysical Research*, *93*(C12), 15467, doi:10.1029/JC093iC12p15467.

Sonu, C. J., S. P. Murray, S. A. Hsu, J. N. Suhayda, and E. Waddell (1973), Sea breeze and coastal processes, *Eos, Transactions American Geophysical Union*, *54*(9), 820, doi:10.1029/EO054i009p00820.

Sorensen, R. M. (1993), *Basic wave mechanics: for coastal and ocean engineers*, John Wiley & Sons Inc, Canda.

Stech, J. L., and J. A. Lorenzzetti (1992), The response of the South Brazil Bight to the passage of wintertime cold fronts, *Journal of Geophysical Research*, *97*(C6), 9507-9520, doi:10.1029/92jc00486.

Stone, G. W., B. Liu, D. A. Pepper, and P. Wang (2004), The importance of extratropical and tropical cyclones on the short-term evolution of barrier islands along the northern Gulf of Mexico, USA, *Marine Geology*, *210*(1-4), 63-78, doi:10.1016/j.margeo.2004.05.021.

Thorpe, S. A. (2005), *The turbulent ocean*, Cambridge University Press, Cambridge.

Ting, F. C. K., and J. T. Kirby (1996), Dynamics of surf-zone turbulence in a spilling breaker, *Coastal Engineering*, *27*(3-4), 131-160, doi:10.1016/0378-3839(95)00037-2.

Tomás, A., F. Méndez, and I. Losada (2012). Bed shear stress during Sant Esteve's storm (26th December 2008) along the Catalonia's coast (NW Mediterranean). In: Mateo, M.A. and Garcia -Rubies,T. (Eds.), assessment of the ecological impact of the extreme storm of Sant Esteve's Day (26 December 2008) on the littoral ecosystems of the north Mediterranean Spanish coasts. Final report (PIEC200430E599). Centrode Estudios Avanzados de Blanes, Consejo Superior de Investigaciones Cientficas, Blanes, 45–54.

Trowbridge, J., and S. Elgar (2001), Turbulence measurements in the surf zone*, *Journal of Physical Oceanography*, *31*(8), 2403-2417, doi:http://dx.doi.org/10.1175/1520-0485(2001)031%3C2403:TMITSZ%3E2.0.CO;2.

Türker, U., and M. S. Kabdaşlı (2006), The effects of sediment characteristics and wave height on shape-parameter for representing equilibrium beach profiles, *Ocean Engineering*, *33*(2), 281-291, doi:10.1016/j.oceaneng.2004.12.016.

Uc-Sánchez, E. (2009), Effects of changes from the beach, on benthic habitats in the port of Progreso, Yucatan, 72 pp, *Instituto Tecnologico de Merida Yucatan Conkal*.

Wang, P., R. A. Davis, and N. C. Kraus (1998), Cross-shore distribution of sediment texture under breaking waves along low-wave-energy coasts, Journal of Sedimentary Research, 68(3), 497-506, doi:10.2110/jsr.68.497.

Williams, E., and J. H. Simpson (2004), Uncertainties in estimates of Reynolds stress and TKE production rate using the ADCP variance method, *Journal of Atmospheric and Oceanic Technology*, *21*(2), 347-357, doi:10.1175/1520-0426(2004)021<0347:uieors>2.0.co;2.

Wolfgang, R. (1987), Examples of calculation methods for flow and mixing in stratified fluids, *Journal of Geophysical Research*, *92*(C5), 5305-5328, doi:10.1029/JC092iC05p05305.

APPENDIX A

Figure A.1. Erosion of the shoreface and abundent shell fragments deposition.

APPENDIX B

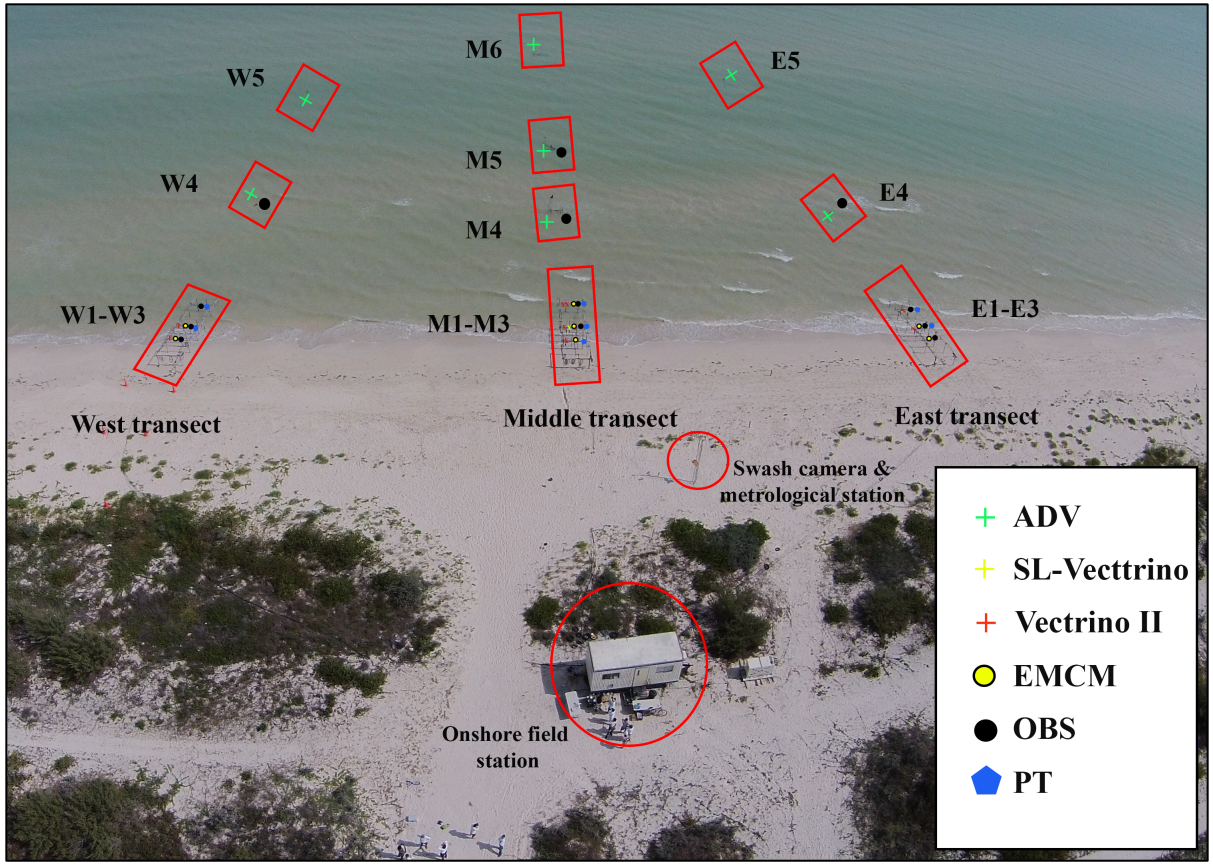

Figure B.1. Landscape view of the field study including all the insturments installed onshore, swash and surf zone

APPENDIX C

Figures C1, C2, C3, and C4 are Timex images, where several frames are overlaid in order to show zones of wave breaking.

Figure C.1. Aerial photography showing the coast and wave conditions for LB time series.

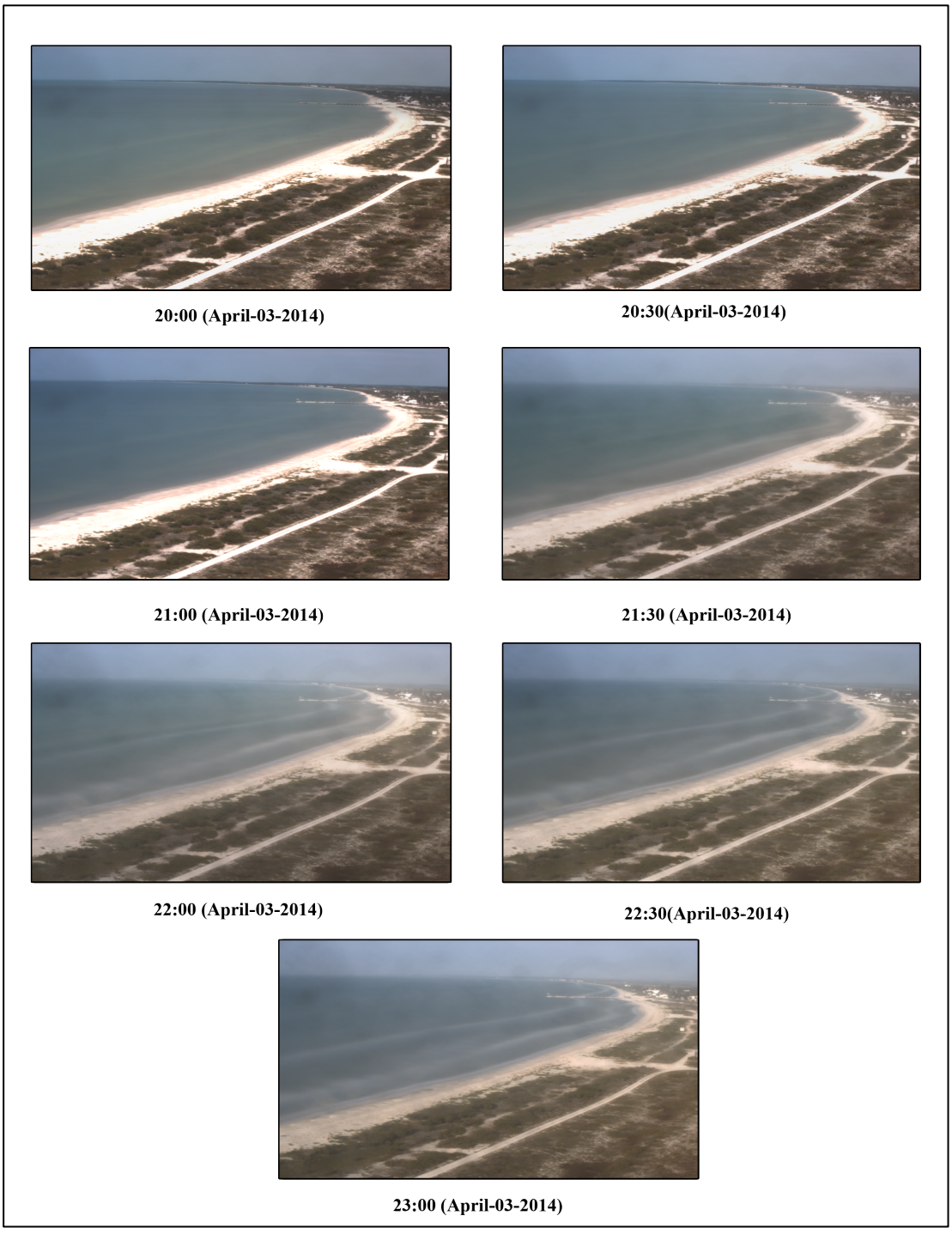

Figure C.2. Aerial photography showing the coast and wave conditions for SB time series.

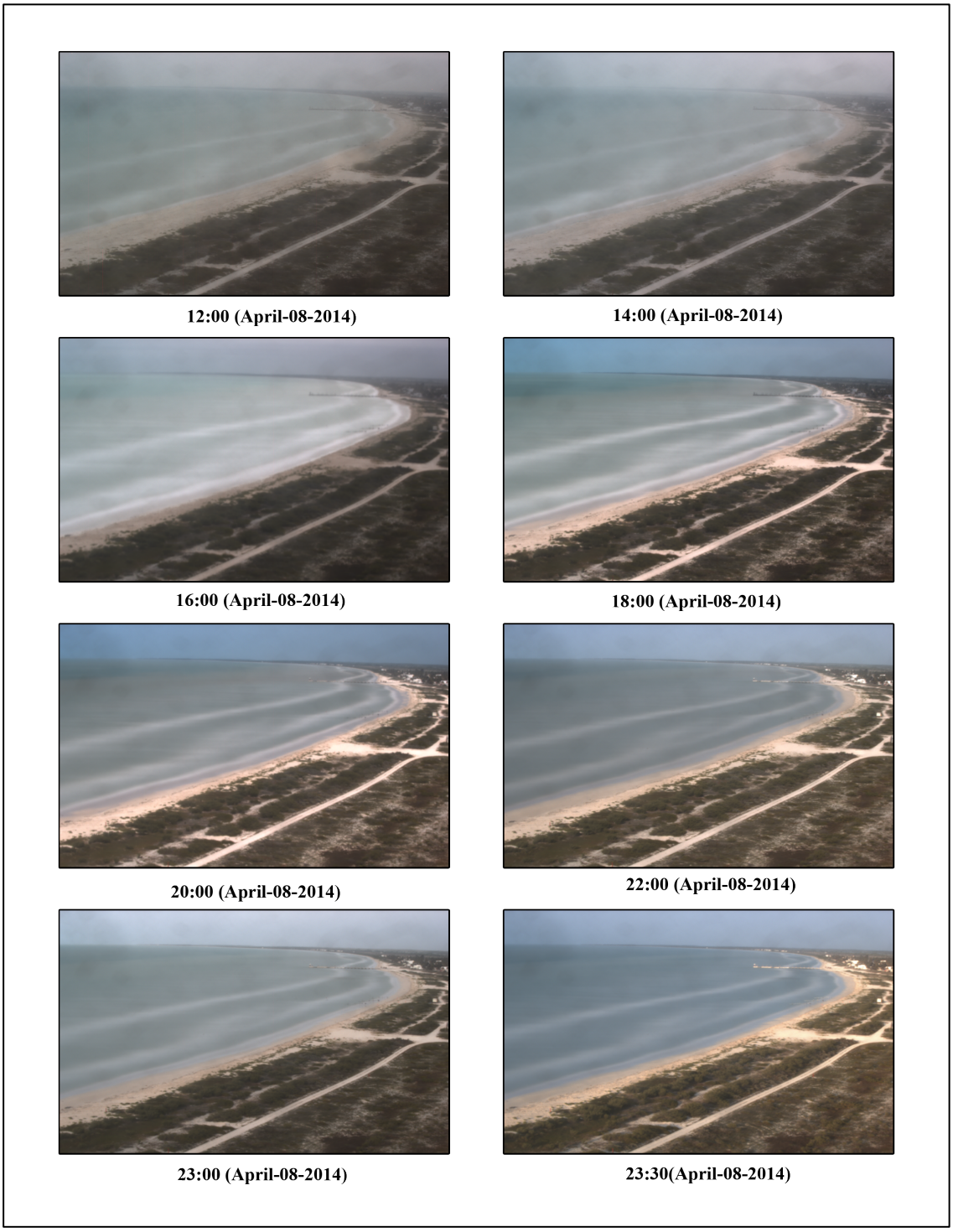

Figure C.3. Aerial photography showing the coast and wave conditions for El-Norte time series on the 8th of April 2014.

12:00 (April-09-2014)

12:30 (April-09-2014)

13:00 (April-09-2014)

Figure C.4. Aerial photography showing the coast and wave conditions for El-Norte time series on the 9th of April 2014.

APPENDIX D

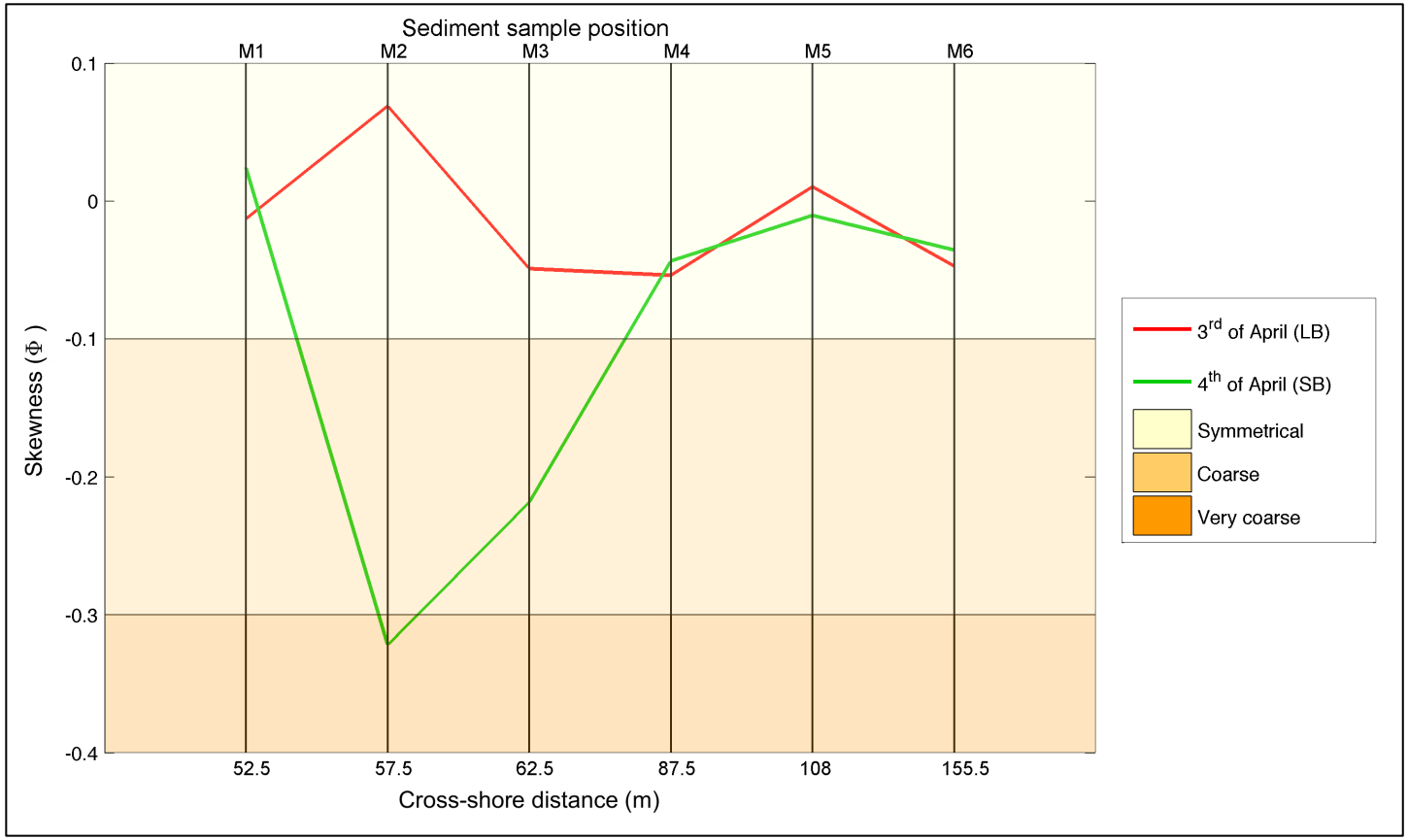

Figure D.1. Estimated skewness for LB and SB for samples collected from M1 to M6.

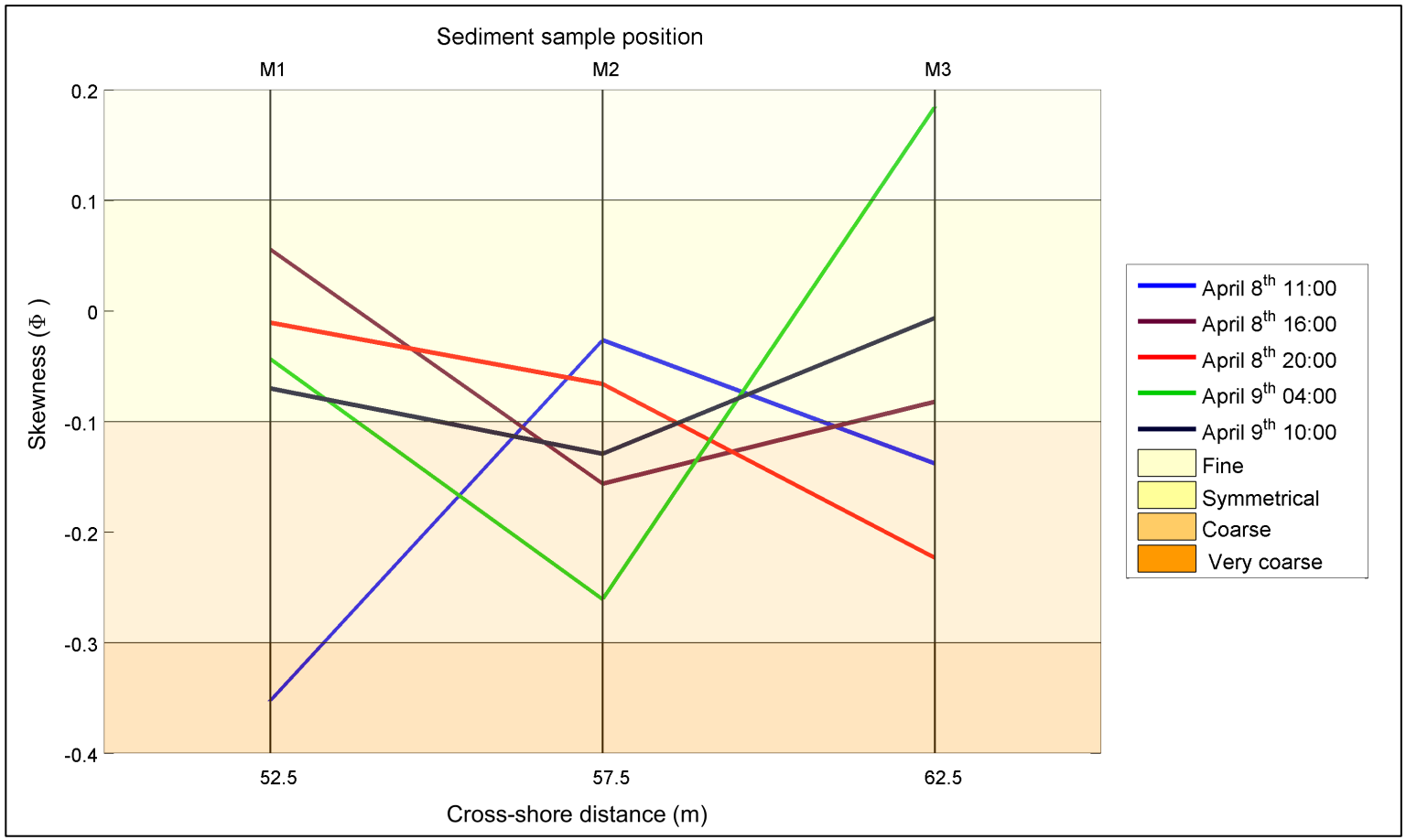

Figure D.2. Estimated skewness during El-Norte for samples collected from M1 to M3.